Grid-Free Localization Algorithm Using Low-Rank Hankel Matrix for Super-Resolution Microscopy

Junhong Min, Kyong Hwan Jin, Michael Unser, *Fellow, IEEE*, and Jong Chul Ye, *Senior Member, IEEE*

***Abstract*— Localization microscopy, such as STORM/PALM, can reconstruct super-resolution images with a nanometer resolution through the iterative localization of fluorescence molecules. Recent studies in this area have focused mainly on the localization of densely activated molecules to improve temporal resolutions. However, higher density imaging requires an advanced algorithm that can resolve closely spaced molecules. Accordingly, sparsity-driven methods have been studied extensively. One of the major limitations of existing sparsity-driven approaches is the need for a fine sampling grid or for Taylor series approximation which may result in some degree of localization bias toward the grid. In addition, prior knowledge of the point-spread function (PSF) is required. To address these drawbacks, here we propose a true grid-free localization algorithm with adaptive PSF estimation. Specifically, based on the observation that sparsity in the spatial domain implies a low rank in the Fourier domain, the proposed method converts source localization problems into Fourier-domain signal processing problems so that a truly grid-free localization is possible. We verify the performance of the newly proposed method with several numerical simulations and a live-cell imaging experiment.**

***Index Terms*— Super-resolution microscopy, annihilating filter, low-rank matrix completion, matrix pencil, source localization.**

I. Introduction

LOCALIZATION microscopy such as STORM/PALM [1]–[3] can achieve super-resolution (SR) imaging beyond the diffraction limit with far-field optics. This breakthrough in the resolution results from the following: 1) the localization precision of a single molecule is not diffraction-limited, and 2) fluorescence molecules can be activated sparsely at each time frame by separating molecules in space and time. Accordingly, non-overlapping activated molecules can be localized to the nanometer accuracy by detecting their centroids. After repeating this process until enough molecules are localized, a final SR image is constructed. However, conventional low-density acquisition schemes are associated with long acquisition times required to collect numerous non-overlapping fluorescent molecules. This compromise between the spatial and temporal resolutions represents the imaging limitation of conventional localization microscopy systems for live-cell imaging.

In order to improve the temporal resolution, high-density (HD) imaging techniques have been developed [4]. They acquired raw data with higher molecular densities such that more molecules can be localized within a time frame, resulting in an accelerated temporal resolution. However, the localization task becomes more difficult because a raw image frame is likely to contain many overlapping PSFs. Several localization methods [4]–[12] have been proposed to resolve closely spaced molecules with overlapping PSFs. These algorithms are mostly based on the use of sparsity in the image domain. For example, multi-emitter fitting methods [4], [5] fit multiple PSFs to the data by increasing the sparsity in a greedy manner. On the other hand, one method [6] used image deconvolution by imposing sparsity-priors such as the Laplacian prior, and another [7] considered more precise statistical models of the camera noise and photo-physics of fluorescence molecules. These deconvolution methods have shown better localization results than previous greedy methods: however, one of the main limitations of the sparsity-driven reconstruction methods is that spatial resolution is limited to the reconstruction grid.

Instead of relying on a finely sampled grid, one study [9] proposed what was termed the FAst Localization algorithm based on a CONtinuous-space formulation (FALCON) for high-density SR microscopy data with the Taylor series approximation of PSFs on a coarser grid. Although these methods can address the problem of high density (HD) localization, there are still many remaining technical issues. For example, FALCON relies on the accuracy of the initial estimation on a fixed grid to establish accurate Taylor series approximations. Therefore, bias remains on the estimated offset, as will be shown later in actual experiments. Second, most existing 2D localization methods use a fixed PSF model which is usually estimated from additional low-density data containing isolated PSFs [6]–[9], [11]. During the early days of localization microscopy, experiments were usually performed on the total internal reflection fluorescence (TIRF) where a single 2D

Manuscript received May 27, 2016; revised December 13, 2016, August 9, 2017, and January 21, 2018; accepted May 17, 2018. Date of publication June 6, 2018; date of current version June 27, 2018. This work was supported by the National Research Foundation of Korea, under Grants NRF-2016R1A2B3008104, NRF-2015M3A9A7029734, and NRF-2017M3C7A1047904. The associate editor coordinating the review of this manuscript and approving it for publication was Prof. Gustavo K. Rohde. *(Corresponding author: Jong Chul Ye.)*

J. Min was with the Department of Bio and Brain Engineering, KAIST, Daejeon 305-701, South Korea. He is now with Samsung Electronics Co., 16677 Suwon, South Korea.

K. H. Jin was with the Department of Bio and Brain Engineering, KAIST, Daejeon 305-701, South Korea. He is now with the Bio Imaging Group, École polytechnique fédérale de Lausanne, 1015 Lausanne, Switzerland.

M. Unser is with the Bio Imaging Group, École polytechnique fédérale de Lausanne, 1015 Lausanne, Switzerland (e-mail: michael.unser@epfl.ch).

J. C. Ye is with the Department of Bio and Brain Engineering, KAIST, Daejeon 305-701, South Korea (e-mail: jong.ye@kaist.ac.kr).

Color versions of one or more of the figures in this paper are available online at http://ieeexplore.ieee.org.

Digital Object Identifier 10.1109/TIP.2018.2843718

PSF model was usually applied to process all of the camera frames. However, more recently, localization microscopy is often implemented using a modified type of TIRF microscopy with the longer depth of field [13]. In addition, there has been growing demand for super-resolution imaging with various experimental protocols, including live-cell imaging. Due to the spatial fluctuations of cells in live-cell imaging, it is expected that the focused region may vary in terms of space and time. Accordingly, the need for localization microscopy data with varying PSF estimations exists to deal with imaging conditions not well-represented by a fixed 2D PSF model [6]–[9], [11]. In addition, for better reconstruction at a low SNR typical in live-cell imaging, a suitable noise and signal model beyond the Gaussian may be incorporated with the imaging algorithm. Finally, there exist inter-frame correlations due to the stochastic physics of the fluorescence probe, which can be exploited to increase the localization accuracy.

In order to address these problems, here we propose a truly grid-free 2D localization algorithm with data-driven local PSF estimation as a penalized maximum likelihood estimator (MLE) under Poisson loglikelihood that can also exploit the temporal correlation of probes. The algorithm is based on the recently proposed annihilating filter-based low-rank Hankel structure matrix approach [14]–[16], which has been successfully applied to many imaging applications, such as MRI [15], [17]–[21], image in-painting [22], image de-noising [23], and nuclear magnetic resonance (NMR) spectroscopy [24], as well as others [25], [26]. This algorithm exploits the special structure of the Fourier spectrum of a signal with a finite rate of innovation (FRI) [27], [28].

More specifically, if the spectral data of the FRI signals is lifted to a Hankel-structured matrix with a suitable weighting, the matrix has a low rank [14], [15], [29]–[32]. Because the fluorophores can be considered to have an infinitesimal size, they can be modeled as delta functions, which are a typical example of FRI signals. Accordingly, the sparsity of activated fluorophores at the nanoscale resolution can be exploited as a low-rank constraint of a Hankel-structured matrix in the spectral domain, which can be used efficiently to deconvolve the data in the Fourier domain. More specifically, the PSF estimation problem can be converted into a spectral weighting estimation problem that finds a parameter that leads to the structure with the lowest rank. Patch-by-patch processing can therefore be performed to track the spatio-temporal variations of PSFs. In contrast to most existing localization algorithms operating on a discrete image grid, our algorithm directly recovers the Fourier coefficients of a sparse signal in a continuous domain. Therefore, the estimation of the fluorescent probe location can be done in a truly grid-free manner using a harmonic retrieval method. Specifically, we estimate spatial positions from the recovered Fourier coefficients by applying a subspace-based harmonic retrieval algorithm known as algebraically coupled matrix pencils (ACMP) [33]. This converts the MLE problem into an all-Fourier-domain formulation under low-rank structured-matrix constraints. Moreover, this Fourier-based approach allows the collaborative reconstruction of multiple consecutive data frames, resulting in higher reconstruction performance.

We are aware of a recent work, which is also based on Fourier-domain processing [11]. Specifically, Hua [34] recovered the Fourier spectrum via direct inverse filtering with a given PSF and then estimated the probe locations by applying a matrix pencil algorithm known as matrix enhancement and matrix pencil (MEMP). Although this method is computationally fast, it is sensitive to noise, as direct inverse filtering generally enhances high frequencies. In addition, it uses a fixed PSF model. In contrast, our method fully utilizes the noise model and adaptively estimates the PSFs, making it more general and more robust.

The paper is organized as follows. We begin with the theory and problem formulation of localization microscopy in Section II. The proposed algorithm is presented in Section III. Then, numerical and experimental results are shown in Section IV. Finally, we discuss several issues and conclude the paper.

II. Mathematical Preliminaries

A. Notation

Throughout the paper, the bold lower-case character (e.g. $\mathbf{x}, \mathbf{y}$) represents a vector. The i-th elements of a vector $\mathbf{x}$ is represented by $x[i]$ or x_i. Moreover, $\mathbf{x}^i$ and $\mathbf{x}_j$ correspond to the i-th row and the j-th column of matrix X, respectively.

A Hankel-structured matrix generated from an n-dimensional vector $\mathbf{x} = [x_1 \cdots x_n]^T \in \mathbb{C}^n$ has the following structure:

$$\mathscr{H}(\mathbf{x}) = \begin{bmatrix} x[1] & x[2] & \cdots & x[d] \\ x[2] & x[3] & \cdots & x[d+1] \\ \vdots & \vdots & \ddots & \vdots \\ x[n-d+1] & x[n-d+2] & \cdots & x[n] \end{bmatrix}. \tag{1}$$

We denote the space of this type of Hankel structure matrices as $\mathcal{H}(n, d)$.

A stream of Dirac impulses is defined by

$$x(t) = \sum_{k=1}^{K} s_k \delta(t - t_k),$$

where $\delta(\cdot)$ denotes the Dirac delta function, and $\{t_k\}$ are the locations of the Dirac impulses. Then, we define its l_0-counting function $\|x\|_0$ by counting the number of Dirac impulses.

B. Forward Model

For the noiseless case, the measurement $u(\mathbf{r})$, $\mathbf{r} \in \mathbb{R}^d$ ($d =$ 2, or 3 for two- or three- dimensional problems, respectively) on the image plane $\mathcal{M}$ through an objective lens can be described by the integral equation:

$$u(\mathbf{r}) = \int_{\mathcal{O}} d\mathbf{r}' a(\mathbf{r}, \mathbf{r}') x(\mathbf{r}'), \quad \mathbf{r} \in \mathcal{M}, \tag{2}$$

where $x(\mathbf{r}')$ denotes a specimen on the object space $\mathcal{O}$, and $a(\cdot, \mathbf{r}')$ is the point-spread function (PSF) from an infinitesimal source at $\mathbf{r}'$. In addition, for fluorescence imaging, $x(\mathbf{r}')$, $\mathbf{r}' \in \mathcal{O}$ can be described by

$$x(\mathbf{r}') = u_{ex}(\mathbf{r}') \eta(\mathbf{r}') \tag{3}$$

where $u_{ex}(\mathbf{r}')$ denotes the optical flux at the excitation wavelength of the fluorophore, and $\eta(\mathbf{r}')$ is the fluorescent yield.

In super-resolution microscopy, fluorescent probes are commonly viewed as infinitesimal point light sources distributed over cell organelles. Therefore, if we consider K-sparse fluorescent probes, the unknown fluorescent distribution can be modeled as a stream of Dirac impulses:

$$x(\mathbf{r}') = \sum_{k=1}^{K} s_k \delta(\mathbf{r}' - \mathbf{r}_k), \tag{4}$$

where s_k denotes the fluorescent intensity. Note that (4) is a special case of FRI signals (see [14], [27] for more details). In the super-resolution microscopy experiments, several temporal frames are acquired, as the fluorescent intensity $\{s_k\}$ changes with the temporal frames.

Thus far, the measurements at all spatial coordinates of the detector plane $\mathcal{M}$ have been modeled. However, in the presence of pixelation, the acquired data consist of the number of detected photons at each pixel. If we consider a pixelated detector with M pixels, the data model describing image acquisition by the m-th detector is then given by

$$u_m = \int_{C_m} d\mathbf{r} \int_{\mathcal{O}} d\mathbf{r}' a(\mathbf{r}, \mathbf{r}') x(\mathbf{r}'), \quad m = 1, \cdots, M \tag{5}$$

where C_m denotes the m-th detector area on $\mathcal{M}$.

C. Existing Penalized Maximum Likelihood Approaches

In most existing approaches, the object space $\mathcal{O}$ is discretized into N voxels so that $\mathbf{x} \in \mathbb{R}^N$ becomes a discretized unknown fluorophore distribution vector. Additionally, Eq. (5) is approximated as

$$u_m \simeq \sum_{j=1}^{N} a_{mj} x_j \tag{6}$$

where

$$a_{mj} = \int_{C_m} a(\mathbf{r}, \mathbf{r}'_j) d\mathbf{r}, \quad x_j = x(\mathbf{r}'_j)$$

and $\mathbf{r}'_j$ denotes the j-th voxel location on the object space. Suppose, furthermore, that $\mathbf{y} \in \mathbb{R}^M$ denote the detector measurements, and $A = [a_{ij}]_{i,j=1}^{M,N}$. Then, the negative loglikelihood function from Poisson intensity measurements is given by:

$$L(\mathbf{x}) = \mathbf{1}^T (A\mathbf{x} + \mathbf{b}) - \mathbf{y}^T \log(A\mathbf{x} + \mathbf{b}) \tag{7}$$

where $\mathbf{b}$ is the background fluorescent distribution originating from the autofluorescence, $\mathbf{1}$ denotes a vector with elements of ones of an appropriate size and $\log(\cdot)$ is treated as an element-by-element operation. Subsequently, the conventional estimation task can be formulated as the following minimization problem:

$$\min_{\mathbf{x}} J(\mathbf{x}) \quad \text{where } J(\mathbf{x}) = L(\mathbf{x}) + pen(\mathbf{x}), \tag{8}$$

where the function $pen(\mathbf{x})$ imposes a penalty to guide the reconstruction.

One of the technical difficulties related to minimizing $L(\mathbf{x})$ in Eq. (7) is the non-separability of the likelihood term, *i.e.* $\log(A\mathbf{x})$. Figueiredo and Bioucas-Dias [35] proposed the PIDAL (Poisson image deconvolution by augmented Lagrangian) algorithm using the alternating direction method of multipliers (ADMM) without approximating the Poisson loglikelihood. In PIDAL, the PSF matrix was assumed to be spatially invariant, allowing the fast Fourier transform (FFT) to be used for rapid computation of matrix vector multiplications.

However, existing deconvolution approaches have limitations on super-resolution microscopy. Firstly, accuracy of the approximation (6) is strongly dependent on the sampling grid, meaning that very fine discretization is required. Secondly, existing approaches usually adopt spatially invariant PSF, which is typically obtained from an additional PSF measurement experiment. Accordingly, these methods cannot take into account the fact that a PSF can vary with the spatial location and time due to the extended acquisition time, movements of the sample, and the instability of the sample holders. Accordingly, the accuracy of existing reconstruction methods can deteriorate.

Below, we use the variable splitting technique of PIDAL for our all-Fourier domain optimization. However, variable splitting is not our main contribution. Specifically, any type of variable splitting method beyond those of PIDAL can be incorporated into our all-Fourier formulations to address the aforementioned problems. For example, the algorithm can be combined with a Poisson ML estimator using a concave-convex procedure (CCCP) [8].

III. Theory

In order to solve the above-mentioned limitations, we propose a Fourier-domain formulation of a penalized ML using the adaptive PSF estimation technique, which allows truly grid-free localization. For the sake of simplicity, we derive the algorithm using a 1-D signal model; the 2D formulation will be discussed later.

A. Fourier-Domain Formulation of Penalized ML

In our approach, (7) is solved in a patch-by-patch manner. However, by estimating the PSF for each patch, a spatially varying PSF can be addressed. Without a loss of generality, the detector pitch is assumed to be 1. Hence, pixelated detector measurement on the m-th detector is modeled by

$$u_m = (p * a * x)(m) = \int_{\mathcal{O}} \int_{\mathcal{O}} dr dr' p(m - r) a(r - r') x(r'),$$

where $*$ denotes a continuous-domain convolution and $p(r)$ is a rectangular function given by

$$p(r) = \begin{cases} 1, & |r| < 1/2, \\ 0, & \text{otherwise.} \end{cases}$$

Therefore, with $\mathbf{u} = [u_1 \cdots u_M]^T$, the penalized ML estimation problem for the estimation of the stream of K- Dirac impulses becomes:

$$\begin{aligned} &\min_{\mathbf{u}} \ \mathbf{1}^T (\mathbf{u} + \mathbf{b}) - \mathbf{y}^T \log(\mathbf{u} + \mathbf{b}) \\ &\text{subject to } u_m = (p * a * x)(m), \quad m = 1, \cdots, M \\ &\qquad \|x\|_0 \le K \end{aligned} \tag{9}$$

where $\|x\|_0$ denotes the number of Dirac impulses.

The minimization problem in (9) is solved using ADMM, as is done in PIDAL [35]. Specifically, the associated Lagrangian is given by

$$L(\mathbf{s},\mathbf{u},\boldsymbol{\lambda}) = \mathbf{1}^T(\mathbf{u}+\mathbf{b}) - \mathbf{y}^T\log(\mathbf{u}+\mathbf{b}) + \frac{\alpha}{2}\sum_{m=1}^{M}|u_m - (p*a*x)(m) + \lambda_m|^2, \quad \|x\|_0 \le K$$

with the corresponding subprograms then as follows:

$$\begin{aligned} z_m^{(k)} &= (p*a*x^{(k)})(m) - \lambda_m^{(k)} \\ u_m^{(k+1)} &= \arg\min_{u_m > -b_m}\left\{u_m - y_m\log(u_m+b_m) + \frac{\alpha}{2}|u_m - z_m^{(k)}|^2\right\} \\ &= \frac{1}{2}\left(z_m^{(k)} - b_m - \frac{1}{\alpha} + \sqrt{\left(z_m^{(k)} + b_m - \frac{1}{\alpha}\right)^2 + \frac{4y_m}{\alpha}}\right) \end{aligned} \tag{10}$$

$$x^{(k+1)} = \arg\min_{x,\|x\|_0\le K}\sum_{m=1}^{M}|u_m^{(k+1)} - (p*a*x)(m) + \lambda_m^{(k)}|^2 \tag{11}$$

$$\lambda_m^{(k+1)} = u_m^{(k+1)} - (p*a*x^{(k+1)})(m) + \lambda_m^{(k)}. \tag{12}$$

Although we use variable splitting in a manner similar to that in PIDAL for Poisson noise, the main difference of the proposed algorithm is that the purpose of the present task is to recover a continuous-domain signal composed of Dirac impulses. Hence, a method to solve subprogram (11) without discretization is required. Accordingly, rather than solving subprogram (11), we convert it to an equivalent Fourier-domain problem. Toward this, we need the following result:

Proposition 1: Suppose that y_m has finite support, i.e. $y_m = 0$ when $m \in \mathbb{Z}\setminus[1,\cdots,M]$ and the detector pitch is 1. Then, we have

$$\sum_{m=1}^{M}|y_m - (p*a*x)(m)|^2 = \frac{1}{2\pi}\int_{2\pi}\left|\hat{y}\left(e^{j\omega}\right) - \sum_{n\in\mathbb{Z}}\hat{p}(\omega+2\pi n)\hat{a}(\omega+2\pi n)\hat{x}(\omega+2\pi n)\right|^2 d\omega. \tag{13}$$

where $\hat{y}\left(e^{j\omega}\right)$ is the discrete time Fourier transform (DTFT) of the sequence y_m; and $\hat{p}(\omega)$, $\hat{a}(\omega)$, and $\hat{x}(\omega)$ are the continuous time Fourier transform (CTFT) of p, a and x, respectively.

Proof: Since the detector pitch is 1, the normalized frequency in DTFT is equal to the frequency in the CTFT domain. Therefore, the effect of the sampling for $(p*a*x)(t)$ is a 2π periodization in the frequency domain. The final step of the proof is to use the Parseval's relationship in DTFT. This concludes the proof. □

If we also assume that the modulation transfer function $\hat{a}(\omega)$ is bandlimited, then the 2π periodic copies do not overlap and Eq. (13) is further simplified to

$$\sum_{m=1}^{M}|y_m - (p*a*x)(m)|^2 = \frac{1}{2\pi}\int_{2\pi}\left|\hat{y}\left(e^{j\omega}\right) - \hat{p}(\omega)\hat{a}(\omega)\hat{x}(\omega)\right|^2 d\omega. \tag{14}$$

Given the bandlimited PSF, even if the spectrum of the stream of Dirac impulses is not bandlimited, (14) still holds. Next, because the y_m signals are assumed to be finite-supported, we can sample the Fourier grid at the Nyquist sampling rate so that

$$\sum_{m=1}^{M}|y_m - (p*a*x)(m)|^2 = A\sum_{k=1}^{M}\left|\hat{y}[k] - \hat{p}[k]\hat{a}[k]\hat{x}[k]\right|^2 \tag{15}$$

where $\hat{y}[k]$, $\hat{p}[k]$, $\hat{a}[k]$ and $\hat{x}[k]$ are sampled value of $\hat{y}\left(e^{j\omega}\right)$, $\hat{p}(\omega)$, $\hat{a}(\omega)$ and $\hat{x}(\omega)$ at $\omega = 2\pi k/M$, respectively. Note that the constant A comes from the frame bound of the sinc interpolation kernel, which is tight. This instance of spectral domain discretization is equivalent to the imposition of the *periodic* repetition onto the image-domain signal. This creates the stream of Dirac impulses periodic with a period of M, which is a mandatory step in the FRI signal model [27]. At this stage, the next question concerns how to impose the continuous-domain constraint $\|x\|_0 \le K$ in the Fourier domain. To do this, we need the following key result from [14]:

Theorem 2 [14]: Let $K+1$ denotes the minimum size of annihilating filters that annihilate the discrete Fourier data $\hat{x}[k]$. Assume that $\min(n-d+1,d) > K$. Then, for a given Hankel-structured matrix $\mathscr{H}(\hat{\mathbf{x}}) \in \mathcal{H}(n,d)$ constructed using $\hat{\mathbf{x}} = [\hat{x}[1],\cdots,\hat{x}[n]]$, we have

$$\text{RANK}\left(\mathscr{H}(\hat{\mathbf{x}})\right) = K, \tag{16}$$

where RANK$(\cdot)$ *denotes a matrix rank.*

Specifically, for the stream of Dirac impulses in (4), the minimum-length annihilating filter $\hat{h}[k]$ has the following z-transform representation [27]:

$$\hat{h}(z) = \sum_{l=0}^{K}\hat{h}[l]z^{-l} = \prod_{j=0}^{K-1}(1 - e^{-i2\pi t_j/\tau}z^{-1}) \tag{17}$$

whose length is $K+1$. Therefore, the associated Hankel matrix should have rank K from Theorem 2. By combining all of these components, the spectral domain formulation of the subprogram (11) is

$$\hat{\mathbf{x}}^{(k+1)} = \arg\min_{\hat{\mathbf{x}}\in C_H}\|\hat{\mathbf{u}}^{(k+1)} - \hat{\mathbf{p}}\odot\hat{\mathbf{a}}\odot\hat{\mathbf{x}} + \hat{\boldsymbol{\lambda}}^{(k)}\|^2 + \lambda\text{RANK}\left(\mathscr{H}(\hat{\mathbf{x}})\right),$$

where C_H denotes the set of Hermitian symmetric spectra because the image-domain counterpart should be real-valued.

Because direct rank minimization is a non-convex optimization problem, we will relax the constraint by minimizing the nuclear norm of this matrix. In this paper, we employ a factorization-based rank minimization algorithm [36] that does not involve the singular value decomposition. The algorithm is based on the following observation [37]:

$$\|A\|_* = \min_{U,V:A=UV^H}\|U\|_F^2 + \|V\|_F^2, \tag{18}$$

where $U \in \mathbb{C}^{(n-d+1)\times r}$, $V \in \mathbb{C}^{d\times r}$ and $r \ge K$ Hence, (11) can be reformulated as the nuclear norm-minimization problem

under the matrix-factorization constraint:

$$\min_{\hat{\mathbf{x}}\in C_H,U,V} \frac{1}{2}\|\hat{\mathbf{y}}-\hat{\mathbf{p}}\odot\hat{\mathbf{a}}\odot\hat{\mathbf{x}}\|^2+\frac{\lambda}{2}\left(\|U\|_F^2+\|V\|_F^2\right)$$
$$\text{subject to } \mathscr{H}(\hat{\mathbf{x}})=UV^H, \tag{19}$$

where $\hat{\mathbf{y}} = \hat{\mathbf{u}}^{(k+1)} + \boldsymbol{\lambda}^{(k)}$. With an additional step of ADMM [38], we have the following cost function:

$$L(U,V,\hat{\mathbf{x}},\Lambda) := \frac{1}{2}\|\hat{\mathbf{y}}-\hat{\mathbf{p}}\odot\hat{\mathbf{a}}\odot\hat{\mathbf{x}}\|^2+\frac{\lambda}{2}\left(\|U\|_F^2+\|V\|_F^2\right)$$
$$+\frac{\mu}{2}\|\mathscr{H}(\hat{\mathbf{x}})-UV^H+\Lambda\|_F^2 \tag{20}$$

One of the advantages of the ADMM formulation is that each subproblem is simply obtained from (20). More specifically, $\mathbf{x}^{(n+1)}$, $U^{(n+1)}$ and $V^{(n+1)}$ can be obtained, respectively, by applying the following optimization problems sequentially:

$$\begin{aligned}
\hat{\mathbf{x}}^{(n+1)} &= \min_{\hat{\mathbf{x}}\in C_H}\frac{1}{2}\|\hat{\mathbf{y}}-\hat{\mathbf{p}}\odot\hat{\mathbf{a}}\odot\hat{\mathbf{x}}\|^2\\
&\quad+\frac{\mu}{2}\|\mathscr{H}(\hat{\mathbf{x}})-U^{(n)}V^{(n)H}+\Lambda^{(n)}\|_F^2\\
U^{(n+1)} &= \arg\min_U \frac{\lambda}{2}\|U\|_F^2+\frac{\mu}{2}\|\mathscr{H}(\hat{\mathbf{x}}^{(n+1)})\\
&\quad-UV^{(n)H}+\Lambda^{(n)}\|_F^2\\
V^{(n+1)} &= \arg\min_V \frac{\lambda}{2}\|V\|_F^2+\frac{\mu}{2}\|\mathscr{H}(\hat{\mathbf{x}}^{(n+1)})\\
&\quad-U^{(n+1)}V^H+\Lambda^{(n)}\|_F^2
\end{aligned} \tag{21}$$

with the Lagrangian update then given by

$$\Lambda^{(n+1)} = \mathscr{H}(\hat{\mathbf{x}}^{(n+1)}) - U^{(n+1)}V^{(n+1)H}+\Lambda^{(n)}.$$

It is easy to show that without the constraint of Hermitian symmetry, the step in (21) results in the following intermediate step

$$\hat{f}^{(n+1)[i]} = \frac{(\hat{a}[i]^*\hat{p}[i]^*\hat{y}[i])+\mu P_i\left(\mathscr{H}^*\left(U^{(n)}V^{(n)H}-\Lambda^{(n)}\right)\right)}{|\hat{a}[i]\hat{p}[i]|^2+\mu P_i(\mathscr{H}^*\mathscr{H}(\mathbf{e}_i))},$$

where $\mathbf{e}_i$ denotes the unit coordinate vector where the i-th element is 1, and P_i is the projection operator of the i-th coordinate. Then, by imposing the Hermitian symmetry constraint, $\hat{\mathbf{x}}^{(n+1)}$ is given as

$$\hat{\mathbf{x}}^{(n+1)} = P_H(\hat{\mathbf{f}}^{(n+1)}),$$

where P_H is the projection operator on a space of matrices with Hermitian symmetry.

The subproblems for U and V are easily solved by taking the derivative with respect to each matrix, and thus we have

$$\begin{aligned}
U^{(n+1)} &= \mu\left(\mathscr{H}(\hat{\mathbf{x}}^{(n+1)})+\Lambda^{(n)}\right)V^{(n)}\left(\lambda I+\mu V^{(n)H}V^{(n)}\right)^{-1}\\
V^{(n+1)} &= \mu\left(\mathscr{H}(\hat{\mathbf{x}}^{(n+1)})+\Lambda^{(n)}\right)^H U^{(n+1)}\\
&\quad\times\left(\lambda I+\mu U^{(n+1)H}U^{(n+1)}\right)^{-1}
\end{aligned}$$

Note that the computational complexity of our ADMM algorithm is dependent on these matrix inversions, whose complexity is determined by the estimated rank of the structured matrix. Therefore, even when the structured matrix is large, the estimated rank can be much smaller, which significantly reduces the overall complexity.

In summary, the original ADMM formulation for the penalized ML formulation can be equivalently converted to the Fourier-domain formulation as follows,

$$\mathbf{z}^{(k)} = \mathcal{F}^{-1}\left(\hat{\mathbf{p}}\odot\hat{\mathbf{a}}\odot\hat{\mathbf{x}}^{(k)}-\boldsymbol{\lambda}^{(k)}\right) \tag{22}$$

$$u_m^{(k+1)} = \frac{1}{2}\left(z_m^{(k)}-b_m-\frac{1}{\alpha}+\sqrt{\left(z_m^{(k)}+b_m-\frac{1}{\alpha}\right)^2+\frac{4y_m}{\alpha}}\right) \tag{23}$$

$$\begin{aligned}
\hat{\mathbf{x}}^{(k+1)} &= \arg\min_{\hat{\mathbf{x}}\in C_H,\mathscr{H}(\hat{\mathbf{x}})=UV^H}\frac{1}{2}\|\hat{\mathbf{u}}^{(k+1)}-\hat{\mathbf{p}}\odot\hat{\mathbf{a}}\odot\hat{\mathbf{x}}\\
&\quad+\hat{\boldsymbol{\lambda}}^{(k)}\|^2+\frac{\lambda}{2}\left(\|U\|_F^2+\|V\|_F^2\right)
\end{aligned} \tag{24}$$

$$\hat{\boldsymbol{\lambda}}^{(k+1)} = \hat{\mathbf{u}}^{(k+1)}-\hat{\mathbf{p}}\odot\hat{\mathbf{a}}\odot\hat{\mathbf{x}}^{(k+1)}+\hat{\boldsymbol{\lambda}}^{(k)} \tag{25}$$

Here, except for the second step, the remaining deconvolution steps are done in the Fourier domain.

Note that the alternating direction method of multipliers (ADMM) is widely used to solve large-scale linearly constrained optimization problems, convex or nonconvex, in many engineering fields. Specifically, the convergence of the ADMM algorithm to minimize the sum of two or more nonsmooth convex separable functions has been well-studied, and Hong and Luo [39] proved the linear convergence of a general ADMM algorithm with any number of blocks under linear constraints. However, (19) is not convex due to the bi-linear term for Hankel matrix factorization using U and V. Therefore, we cannot directly use the results by Hong and Luo [39]. For nonconvex problems, we are aware that Hong *et al.* [40] and Li and Pong [41] showed that the ADMM algorithm converges to the set of stationary solutions, but our problem does not fit this setting. Therefore, rather than claiming a convergence guarantee in relation to our problem, here we rely on our empirical results, which consistently show the convergent behavior. The rigorous proof of the convergence is important but beyond the scope of the current paper.

B. Advantages of Fourier-Domain Formulation

There are several important advantages when using the Fourier-domain formulation of a penalized ML. First, if there are variations of 2D PSF functions with small z-directional fluctuations in the fluorophore distribution, we can easily estimate the varying 2D PSF by means of spectral domain processing. More specifically, the most widely used 2D PSF model is Gaussian function. Specifically, a symmetric Gaussian function is used so that different PSFs can be created by adjusting a single parameter σ. Accordingly, the Gaussian PSF model is given with the following approximation:

$$h_\sigma \simeq p * a$$

where the single parameter σ is determined by an optical set-up as well as a slight variation of axial locations of probes.

In noiseless case, the Fourier domain spectrum $\hat{x}_\sigma[k]$ can be then obtained by applying an inverse filter

$$\hat{x}_\sigma[k] = \frac{\hat{y}[k]}{\hat{h}_\sigma[k]}, \tag{26}$$

where $\hat{h}_\sigma[k]$ denotes the Fourier spectrum of h_σ. As we have already shown, the sparsity of the continuous-domain signal $x(r)$ can be equivalently represented by the low-rankness of the Hankel matrix, which is constructed from spectral domain samples. Therefore, we search the parameter σ that minimizes the rank of the Hankel matrix $\mathscr{H}\{\hat{\mathbf{x}}_\sigma\}$:

$$\sigma_o = \arg\min_{\sigma>0} \text{RANK}\left(\mathscr{H}\{\hat{\mathbf{x}}_\sigma\}\right), \tag{27}$$

which provides the optimal parametric PSF estimation.

The second advantage of the Fourier-domain formulation is that the initialization of the U and V matrices can be readily combined with the PSF estimation. In (20), the column dimensions of U and V represent the upper-bound of the rank of the Hankel matrix. Therefore, they should be properly estimated. For the initialization of the U and V matrices, instead of using an inverse filter as in (26), a Wiener filter is used to avoid noise boosting in order to estimate the denoised spectral data:

$$\hat{x}_w[k] = \frac{\hat{h}^*_{\sigma_o}[k]\hat{y}[k]}{|h_{\sigma_o}[k]|^2 + \epsilon}.$$

with an appropriate value of $\epsilon > 0$. The initial U and V matrices are then obtained as a low-rank factorization of $\mathscr{H}\{\hat{\mathbf{x}}_w\}$ by monitoring its singular-value spectrum.

Lastly, after the deconvolution, the algorithm provides an accurate localization model and an optimization framework, enabling truly grid-free localization. Unlike FALCON, which relies on the accuracy of fixed grid guesses to make accurate Taylor series approximations, the proposed localization steps using the matrix pencil method are accurate without the need for precise initialization. Specifically, when a complete set of Fourier coefficients is returned by means of deconvolution, the remaining task corresponds to the harmonic retrieval problem [33], [34], [42], [43]. For example, 1-D harmonic retrieval can be handled by a subspace-based method such as ESPRIT (estimation of signal parameters via rotational invariant techniques) [42] by exploiting the inherent Vandermonde structure of a Hankel matrix constructed using $\hat{\mathbf{x}}$. This Vandermonde structure, in general, can be extended to higher dimensions as well. For the 2D problem, the MEMP (matrix enhancement and matrix pencil) algorithm [34] can be used. The MEMP algorithm solves rank deficiency problem by constructing a lifted matrix, i.e. Hankel matrix [34]. Specifically, it divides the problem into different sequential 1D harmonic problems with matrix pencils, after which it pairs two sets of harmonics in each dimension. Given that this pairing requires an additional minimization step, the use of what are known as algebraically coupled matrix pencils (ACMP) [33] has been proposed to solve the pairing issue. Thus, the ACMP algorithm is used in this paper. As a result, our method can significantly improve the localization accuracy, especially in experimental conditions with low SNRs. Confirmation of this benefit is augmented later in the paper, specifically in the experimental section.

IV. Algorithm Implementation

Based on the theoretical derivation in the previous section, we now provide a more detailed implementation of the algorithm for our 2D super-resolution microscopy problem. As shown in Fig. 1, a raw frame is initially divided into several overlapping patches of 45×45 pixels, where the outermost five pixels of each patch overlap the neighboring patches (the localization results from the overlapped region are excluded from the final results). The following three steps are then applied to each patch: 1) PSF estimation using a low-frequency signal, 2) spectral domain deconvolution to retrieve Fourier data $\hat{\mathbf{x}}$ under a Poisson noise model, and 3) fluorophore location estimation using the harmonic retrieval approach. Additional details pertaining to each step are given below.

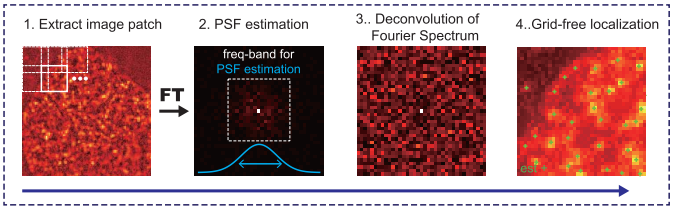

Fig. 1. Schematic representation of the proposed method.

A. Parametric PSF Estimation

As noted earlier, we use the simple 2D-symmetric Gaussian model $h_\sigma(\mathbf{r}) = e^{-\frac{\|\mathbf{r}\|^2}{2\sigma^2}}$ with the parameter σ to describe the shape of the 2D PSF. The validity of using Gaussian PSF approximation under our experimental set-up is discussed in Appendix. Because the measurement y is contaminated by noise, we need two small modifications to increase the degree of noise robustness. First, to apply the inverse filter as in (26), we only use the low-frequency part of $\hat{y}[k]$ to improve the signal-to-noise ratio of our filtering procedure. Specifically, we took 17×17 coefficients for all our numerical and experimental calculations. Second, due to the noise contaminations, $\mathscr{H}\{\hat{\mathbf{x}}_\sigma\}$ becomes a full rank matrix regardless of the parameter σ. Hence, instead of using (27), we rely on a Schatten-p quasi-norm as a rank surrogate:

$$\sigma_o = \arg\min_{\sigma} \left\|\mathscr{H}\left\{\hat{\mathbf{x}}_\sigma\right\}\right\|_p^p, \quad 0 < p < 1, \tag{28}$$

after normalizing the MTF function $\|\hat{\mathbf{h}}_\sigma\|_2 = 1$. We recall that the Schatten-p matrix norm of a matrix A is defined as the l_p-norm for singular values:

$$\|A\|_p^p = \sum_n \lambda_n^p,$$

where λ_n denotes the n-th singular value of A. Here, the Schatten p-norm is used as an alternative measure of rank in order to find the σ value which gives the norm with the lowest value. When $p < 1$, the Schatten p-norm is concave and can therefore be used as a better rank surrogate function than the nuclear norm. Because (28) accomplishes single-variable nonlinear optimization, it is solved efficiently by using the built-in MATLAB function **fminbnd**.

B. Deconvolution Step

1) Construction of 2D Hankel Matrices: In the previous section, the deconvolution formula for the 1D signal was derived for simplicity. Nevertheless, the formula for the 2D signal case can easily be extended with a few minor modifications. Let us assume that the variables of $\mathbf{z}, \hat{\mathbf{p}}, \hat{\mathbf{x}}$ in our algorithm are lexicographically ordered vectors. For example, $\hat{\mathbf{x}}$ is a lexicographically ordered vector from the 2D spectrum $\hat{X}$:

$$\hat{X} = [\hat{\mathbf{x}}_1, \cdots, \hat{\mathbf{x}}_n], \quad \hat{\mathbf{x}} = \mathrm{vec}(\hat{X}).$$

In this case, the remaining task is to redefine $\mathscr{H}(\hat{\mathbf{x}})$ as a 2D Hankel matrix of $\hat{X}$. As described in several works [15], [17], [18], the 2D low-rank Hankel matrix originates from 2D annihilating filters; accordingly, for a given annihilating filter of size $d_m \times d_n$, the associated 2D Hankel matrix is given by

$$\mathscr{H}(\hat{\mathbf{x}}) = \begin{bmatrix} \mathscr{H}(\hat{\mathbf{x}}_1) & \mathscr{H}(\hat{\mathbf{x}}_2) & \cdots & \mathscr{H}(\hat{\mathbf{x}}_{d_n}) \\ \mathscr{H}(\hat{\mathbf{x}}_2) & \mathscr{H}(\hat{\mathbf{x}}_3) & \cdots & \mathscr{H}(\hat{\mathbf{x}}_{d_n+1}) \\ \vdots & \vdots & \ddots & \vdots \\ \mathscr{H}(\hat{\mathbf{x}}_{n-d_n+1}) & \mathscr{H}(\hat{\mathbf{x}}_{n-d_n+2}) & \cdots & \mathscr{H}(\hat{\mathbf{x}}_n) \end{bmatrix}, \tag{29}$$

where $\mathscr{H}(\hat{\mathbf{x}}_i) \in H(m, d_m)$ is defined in (1). Then, we can use the same formulation (22)-(25) by replacing the Hankel matrix with the 2D one in (29).

In practice, the background autofluorescence signals b_m should be estimated before the deconvolution step. Here, we use the iterative wavelet threshold method proposed in FALCON [9]. Specifically, assuming that the background signal is spatially smooth, the method finds, at each iteration, a low-resolution image of background autofluorescence by means of a multi-level wavelet transform operation and then subtracts the intensities of the raw image through the low-resolution image. Details pertaining to this step are available in [9].

The values of the parameters λ, α, μ in this step are fixed as follows: $\lambda = 20$, $\alpha = 1e^{-2}$, and $\mu = 1e^{-4}$. For a better upper bound of the rank of the Hankel matrix, we undertake the factorization of $U^{(n)}, V^{(n)}$ from the estimated $\mathscr{H}(\hat{\mathbf{x}}^{(n)})$ and its singular value distribution at every 30 iterations.

2) Extension to Multi-Frame Formulation: In localization microscopy, fluorescence molecules can be activated in several consecutive frames due to the stochastic photo-physics. In other words, activated fluorescent probes have the common supports in these successive frames [44]. This joint sparsity can be also incorporated in our deconvolution framework to improve the quality of the reconstruction. In particular, we can impose joint sparsity by minimizing the rank of the 2D Hankel matrices concatenated side by side [15], [17], [18]. Due to the existence of inter-channel annihilating filters originated from the joint sparsity condition, the rank of the concatenated matrix is small such that we can exploit the low-rankness characteristic. Additional details are given in [15].

This multi-frame version of the problem is nearly identical to that discussed earlier, except for the low-rank regularization term. Specifically, (20) is reformulated as:

$$\begin{aligned} L(U, V, \{\hat{\mathbf{x}}_{(i)}\}_{i=1}^T, \Lambda) := & \sum_{t=0}^{T} \frac{1}{2} \|\hat{\mathbf{y}}_{(t)} - \hat{\mathbf{p}} \odot \hat{\mathbf{a}} \odot \hat{\mathbf{x}}_{(t)}\|^2 \\ & + \frac{\lambda}{2} \left(\|U\|_F^2 + \|V\|_F^2 \right) \\ & + \frac{\mu}{2} \|\mathscr{H}(\{\hat{\mathbf{x}}_{(i)}\}_{i=1}^T) - UV^H + \Lambda\|_F^2 \end{aligned} \tag{30}$$

where T is the number of adjacent frames to be processed simultaneously, $(\cdot)_{(t)}$ denotes a variable at frame t, and the concatenated 2D Hankel matrices is given by

$$\mathscr{H}(\{\hat{\mathbf{x}}_{(i)}\}_{i=1}^T) = [\mathscr{H}(\hat{\mathbf{x}}_{(1)}), \cdots, \mathscr{H}(\hat{\mathbf{x}}_{(T)})].$$

Here, the update of $\hat{\mathbf{x}}$ is modified as:

$$\begin{aligned} & \hat{\mathbf{x}}_{(t)}^{(n+1)} = P_H(\hat{\mathbf{f}}_{(t)}^{(n+1)}), \\ & \hat{f}_{(t)}^{(n+1)}[i] \\ & \quad = \frac{(\hat{a}[i]^* \hat{p}[i]^* \hat{y}_{(t)}[i]) + \mu P_{t,i} \left(\mathscr{H}^* \left(U^{(n)} V^{(n)H} - \Lambda^{(n)} \right) \right)}{|\hat{a}[i]\hat{p}[i]|^2 + \mu P_{t,i}(\mathscr{H}^* \mathscr{H}(\mathbf{e}_i))}. \end{aligned}$$

In this equation, $P_{t,i}$ is the projection operator for the i-th coordinate at frame t.

When we apply the multi-frame deconvolution to raw frames, patches of consecutive T frames are selected in a sliding-window manner. The regularization parameter λ is set to $\lambda = 20/T$.

C. Grid-Free Source Localization Using the Matrix Pencil Method

Once the entire Fourier spectrum $\hat{X}$ is restored, the remaining task is to extract the harmonics from the Fourier spectrum from which the spatial locations can be computed. Specifically, let (x_k, y_k), $k = 1, \cdots, K$ denote the locations of the K-harmonics. The discretized Fourier data is then given by

$$\hat{X}[m, n] = \sum_{k=1}^{K} s_k p_k^m q_k^n,$$

where $p_k = e^{-j\omega x_k}$, $q_k = e^{-j\omega y_k}$. Then, the matrix of Fourier coefficients $\hat{X} \in \mathbb{C}^{m \times n}$ can be decomposed as follows:

$$\hat{X} = PSQ^T,$$

where $S^{K \times K} = \mathrm{diag}\{s_1, \cdots, s_K\}$ is a diagonal matrix. $P \in \mathbb{C}^{m \times K}$, $Q \in \mathbb{C}^{n \times K}$ are Vandermonde structured matrices:

$$P = \begin{bmatrix} 1 & 1 & \cdots & 1 \\ p_1 & p_2 & \cdots & p_K \\ \vdots & \vdots & \ddots & \vdots \\ p_1^{m-1} & p_2^{m-1} & \cdots & p_K^{m-1} \end{bmatrix},$$

$$Q = \begin{bmatrix} 1 & 1 & \cdots & 1 \\ q_1 & q_2 & \cdots & q_K \\ \vdots & \vdots & \ddots & \vdots \\ q_1^{n-1} & q_2^{n-1} & \cdots & q_K^{n-1} \end{bmatrix}.$$

If there are common harmonics in each dimension, we cannot obtain the individual harmonics directly from $\hat{X}$ because

the rank of $\hat{X}$ is less than K. The ACMP [33] algorithm also applies the matrix pencil technique to Hankel-structured matrices to avoid the rank deficiency problem. The MEMP algorithm uses a doubly block Hankel matrix as the lifted matrix, but doing so requires an additional pairing step. The ACMP algorithm solves this pairing issue by constructing a simple block Hankel matrix $Z \in \mathbb{C}^{d_n(m-d_m)\times d_m(n-d_n)}$ from $\hat{X}$, as

$$Z = \begin{bmatrix} \hat{X}^{(1,1)} & \hat{X}^{(2,1)} & \cdots & \hat{X}^{(d_m,1)} \\ \hat{X}^{(1,2)} & \hat{X}^{(2,2)} & \cdots & \hat{X}^{(d_m,2)} \\ \vdots & \vdots & \ddots & \vdots \\ \hat{X}^{(1,d_n)} & \hat{X}^{(2,d_n)} & \cdots & \hat{X}^{(d_m,d_n)} \end{bmatrix},$$

where the block component $Z_{ij} = \hat{X}^{(i,j)}$ is a sub-matrix of $\hat{X}$ given by $\hat{X}^{(i,j)}$, as shown at the bottom of the next page. The block Hankel matrix Z is decomposed as

$$Z = \tilde{P} C \tilde{Q}^T,$$

where $\tilde{P} \in \mathbb{C}^{d_n(m-d_m)\times K}$ and $\tilde{Q} \in \mathbb{C}^{d_m(n-d_n)\times K}$ also have the Vandermonde structure:

$$\tilde{P} = [P_{m-d_m}^T,\ W_Q P_{m-d_m}^T, \cdots,\ W_Q^{d_n-1} P_{m-d_m}^T]^T,$$
$$\tilde{Q} = [Q_{n-d_n}^T,\ W_P Q_{n-d_n}^T, \cdots,\ W_P^{d_m-1} Q_{n-d_n}^T]^T.$$

The diagonal matrices $W_P = \mathrm{diag}\{p_1, p_2, \cdots, p_K\}$ and $W_Q = \mathrm{diag}\{q_1, q_2, \cdots, q_K\}$ contain all harmonic components in each dimension, respectively. $P_{m-d_m} \in \mathbb{C}^{(m-d_m)\times K}$ and $Q_{n-d_n} \in \mathbb{C}^{(n-d_n)\times K}$ are given by

$$P_{m-d_m} = \begin{bmatrix} 1 & 1 & \cdots & 1 \\ p_1 & p_2 & \cdots & p_K \\ \vdots & \vdots & \ddots & \vdots \\ p_1^{m-d_m-1} & p_2^{m-d_m-1} & \cdots & p_K^{m-d_m-1} \end{bmatrix},$$

$$Q_{n-d_n} = \begin{bmatrix} 1 & 1 & \cdots & 1 \\ q_1 & q_2 & \cdots & q_K \\ \vdots & \vdots & \ddots & \vdots \\ q_1^{n-d_n-1} & q_2^{n-d_n-1} & \cdots & q_K^{n-d_n-1} \end{bmatrix}.$$

In order to utilize this Vandermonde structure, the three sub-matrices Z^{tl}, Z^{tr} and $Z^{bl} \in \mathbb{C}^{d_n(m-d_m-1)\times d_m(n-d_n-1)}$ of Z are constructed by omitting the outermost column and row of every block of Z. For example, the (i, j)-th block of Z^{tl} is equal to the top-left sub-matrix of Z_{ts}:

$$Z_{ij}^{tl} = \underline{Z_{ij}|},$$

where $(\cdot)|$ and $\underline{(\cdot)}$ are operations which function to delete the last column of $(\cdot)$ and the last row of $(\cdot)$, respectively. In a similar manner, the top-right Z^{tr} and bottom-left Z^{bl} are defined. Due to the Vandermonde structure, the following two matrix pencils; $Z^{tr} - \alpha Z^{tl}$, $Z^{bl} - \beta Z^{tl}$, have the following properties:

$$Z^{tr} - \alpha Z^{tl} = \underline{\tilde{P}} S \left(W_Q - \alpha I\right) \underline{\tilde{Q}}^T,$$
$$Z^{bl} - \beta Z^{tl} = \underline{\tilde{P}} S \left(W_P - \beta I\right) \underline{\tilde{Q}}^T.$$

where α, β are scalar values. The ACMP algorithm estimates the diagonal matrices W_P and W_Q from these matrix pencils, after which the locations $\{x_k\}_{k=1}^K$ and $\{y_k\}_{k=1}^K$ are found from W_P and W_Q, respectively.

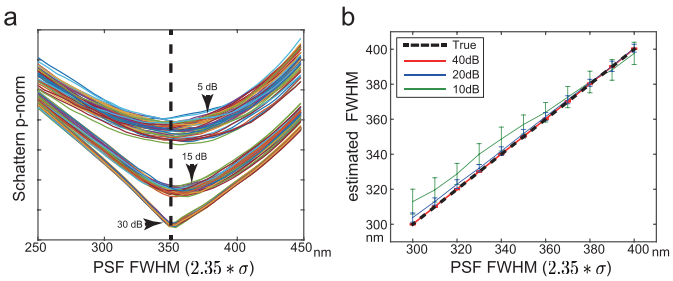

Fig. 2. Performance analysis of the parametric PSF estimation. (a) The values of Schatten norm $\|\mathscr{H}\{\hat{\mathbf{x}}_\sigma\}\|_p^p$ with $p = 0.6$ are plotted along different PSF widths in terms of FWHM ($\simeq 2.35\sigma$). The dotted vertical black line denotes the true FWHM. (b) Averaged estimation errors are plotted along different PSF widths (300 – 400 nm) under three SNR conditions (5dB, 15dB, 30dB). The error bars indicate standard deviations of the errors. For each simulation setting, the analysis was repeated 30 times.

In our implementation, in order to reduce false-positive localizations, the rank of Z is determined by its singular value distribution; in particular, small singular values less than 5% of the maximum are discarded.

V. Results

We analyzed the performance of the proposed algorithm using both numerical and actual experimental results. For a fair comparison, the proposed method was evaluated with two recently developed localization algorithms for the HD imaging: FALCON [9] and DeconSTORM [7]. For a quantitative evaluation, we used several metrics which are regularly used in [9], [10], [45], and [46]. Note that localization-based analysis measures such as the recall rate are not sufficient to evaluate localized results in HD imaging, as localized particles have matching ambiguities. In particular, we observed that the scores for the recall rate and localization errors were not simply converted to the quality of reconstructed super-resolution image. Thus, as in [9], [10], [45], and [46] we also used image-based analysis such as peak-signal-to-noise ratio (PSNR).

A. Numerical Experiments

First, the numerical performances of the parametric PSF estimation were verified, as shown in Fig. 2. Here, we produced HD images of 45×45 pixels, where 35 randomly placed molecules were convolved with a given PSF with the background signals of 20 photons added. To meet the requirements of Poisson noise model, the brightness of the fluorescent molecules was properly adjusted according to the signal-to-noise ratio (SNR). For each simulation setting, 30 simulated images were used. From the simulated images with a given PSF, we measured values of the Schatten p-norm $\|\mathscr{H}\{\hat{\mathbf{x}}_\sigma\}\|_p^p$ with $p = 0.6$ and various values of σ. As expected, the true value of σ led to the minimum values of the Schatten norm when no noise was present in the measurement. In addition, the algorithm was still robust to noise, as shown in Fig. 2 (a). The accuracy of the method was also quantitatively investigated under different noise levels and PSF widths, as shown in Fig. 2 (b). Estimation errors were calculated for three

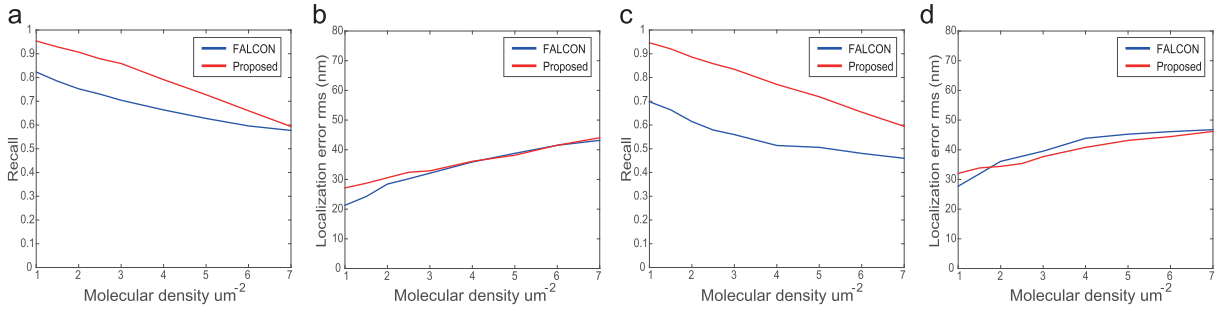

Fig. 3. Localization performances of the proposed method compared to FALCON along a wide range of imaging densities ($1-7\ \mu\mathrm{m}^{-2}$). The simulated images were generated with random distributions of molecules. The results were evaluated by means of recall rates (a,c) and localization errors in terms of root mean square (rms) (b,d). (a,b) correspond to the results in the higher photon-emission case (500,200), and (c,d) correspond to the lower photon-emission (300,150) in terms of (mean, std).

different SNR conditions (5dB, 15dB, and 30dB) within a typical range of PSF widths (300−400 nm) used in localization microscopy. The results showed that most estimation errors were below 20 nm in terms of the full width at half maximum (FWHM), which is an acceptable level in localization microscopy.

We then evaluated the localization performance of the proposed algorithm over a wide range of imaging densities. For this analysis, HD images of 80×80 pixels were generated where K molecules were randomly placed in a central 70×70 area. Here, a fixed PSF was used. In order to consider realistic live-cell imaging conditions, the simulation images were generated at two different photon-emission rates (or brightness) of activated molecules: 500/200 and 300/150 in terms of the mean/standard deviation of log-normal distributions. Additionally, 50 background fluorescent photons were added at every pixel. By assuming a state-of-the-art camera such as an EMCCD (Electron multiplying charge-coupled device) or a sCMOS (scientific complementary metal oxide semiconductor) camera, we initially generated camera shot noises following Poisson distributions, after which small Gaussian noises with variance of 1 were added as camera readout noise.

We measured localization errors with respect to the root mean square (rms), and recall rates ($= \frac{K_{match}}{K}$), where K_{match} is the number of the matched positions and K is the total number of locations. In the analysis, the localized particles with the error exceeding 300 nm - the FWHM of the simulated PSF - were excluded from the analysis. The proposed algorithm was evaluated in comparison to FALCON. DeconSTORM was not included in this analysis because it only provides deconvolution images rather than the localized positions.

The results of the numerical experiments in Fig. 3 show that the proposed algorithm offers significant improvements in the recall rates with comparable accuracy levels. Specifically, the improvement of the recall rates in the case with the lower SNR case shown in Fig. 3 (c-d) is more distinct. While FALCON showed noticeable decreases in the recall rates with lower SNRs, the proposed method retained its good detection capability. The proposed method resulted in lower accuracy in a low-density range because it detected many molecules with low brightness levels.

The final spatial resolution is determined not only by localization errors but also by recall rates. For a better understanding of this effect, we analyzed the performances of the proposed method on two specific geometric structures, as shown in Figs. 4 and 5. First, we produced a radial phantom consisting of equi-angular spaced lines with an angular period of 20°. For each simulated image frame, 15 molecules were newly activated on these lines. Moreover, to impose temporal redundancy of the molecules, the probability of deactivation in the next frame was set to 0.5. In other words, the average activation length of the molecules was two frames. The photon emission rates was set to 500/200 in terms of the mean/standard deviation, and 50 background photon were added. Three localization methods were used to reconstruct the 6000 frames simulated here. Moreover, we measured line profiles for a more quantitative evaluation. The line profiles are averaged for each angular period. As shown in Fig. 4 (g-h), the proposed multi-frame deconvolution algorithm provided a better resolution of a smaller gap between two adjacent lines as compared to the other algorithms. The results also confirmed that using joint sparsity increases the reconstruction quality, which results in the highest PSNR value.

We also conducted experiments with a honeycomb-structured sample, as shown in Fig. 5 (a). In order to simulate the effect of a sample moving along the axial direction, we controlled the widths of the PSF according to a sinusoidal profile as shown in Fig. 5 (f). For this analysis, 1000 HD frames were generated and 50 activated molecules were randomly distributed on the sample in each frame. The photon-emission rates were adjusted in the same manner used in the previous numerical study of the radial phantom, but the

$$\hat{X}^{(i,j)} = \begin{bmatrix} \hat{X}[i,j] & \cdots & \hat{X}[i,j+n-d_n-1] \\ \hat{X}[i+1,j] & \cdots & \hat{X}[i+1,j+n-d_n-1] \\ \vdots & \ddots & \vdots \\ \hat{X}[i+m-d_m-1,j] & \cdots & \hat{X}[i+m-d_m-1,j+n-d_n-1] \end{bmatrix}.$$

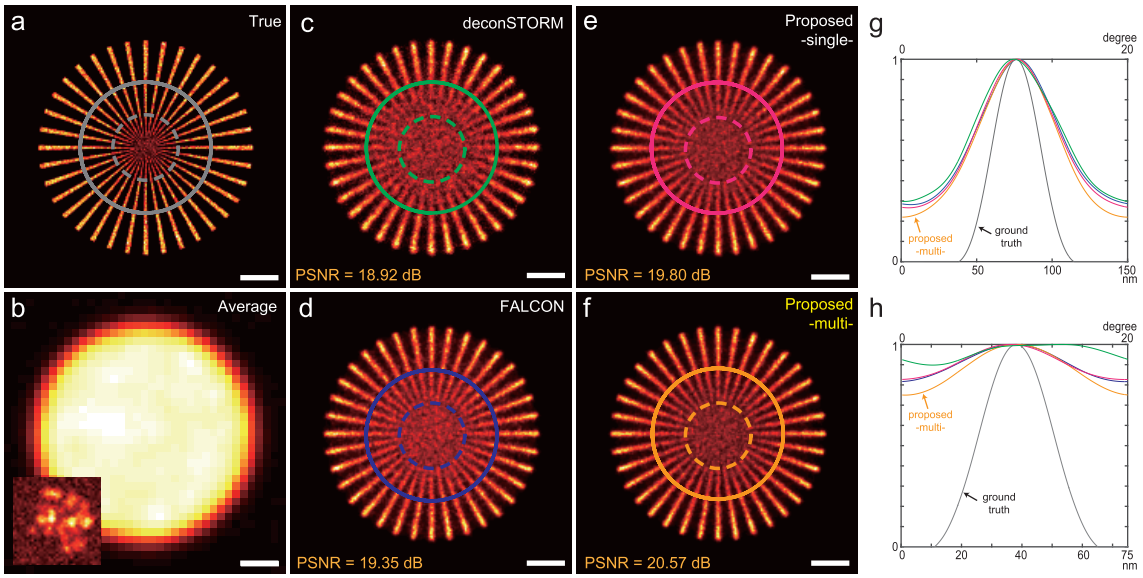

Fig. 4. Performance analysis for a phantom with equi-angularly spaced lines. The angle between two neighboring lines is 20 degree. 6000 high density images were generated where an average of 30 molecules are activated in each frame. A mean activation length of the molecules was set to 2 frames. (a) An SR image generated from true particle distributions. (b) A conventional diffraction-limited image with a single simulated image. (c) An SR image reconstructed by DeconSTORM. (d) An SR image reconstructed by FALCON. (e-f) SR images reconstructed by the proposed method using single frame deconvolution and multi-frame deconvolution, respectively. (g) Line profiles as measured from the solid lines in (a, c-f). (h) Line profiles as measured from the dashed lines in (a, c-f). (g-h) The measured line profiles are averaged at every angular period (=20 degree), and colors of the profiles correspond to the colors of the circles in (a,c-f), respectively. Scale bars in (a-f) are 500 nm.

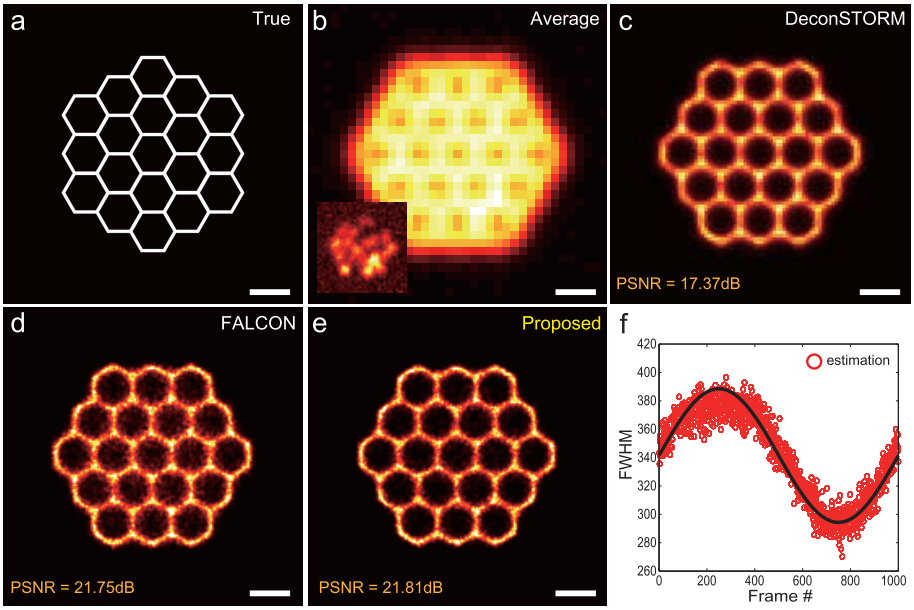

Fig. 5. Performance analysis for a honeycomb structured phantom. 1000 high density images were generated with 50 particles randomly distributed on the phantom for every frame. The PSF width varies along the frames with a sinusoidal profile. (a) An SR image of the phantom. (b) A conventional diffraction-limited image with a single simulated image. (c) DeconSTORM image. (d-e) SR images reconstructed by FALCON and the proposed method, respectively. (f) Results of our PSF estimation, where the black line denotes true PSF widths and the red circles corresponds to the estimated values. Scale bars are 500 nm in (a-e).

temporal redundancy was not considered here. DeconSTORM and FALCON used a fixed PSF corresponding to the average width, while the proposed method used the PSFs estimated in a frame-by-frame manner. These results show that the proposed method accurately estimates variations of the PSF while also retaining the fine details of the structure. On the other hand, FALCON had many false positive localizations and the SR image of DeconSTORM was blurred. The evaluation of the PSNR also confirmed the superiority of our approach.

B. Live-Cell Experiments

The same algorithms were also applied to experimental live-cell imaging data. Specifically, U2OS cells were prepared, and the nuclei of the cells were labeled with Picogreen (1:500 dilution from the original stock of Quant-iT PicoGreen; Invitrogen). dSTORM imaging [47] was performed on an inverted microscope (Axio Observer.D1; Zeiss) equipped with a Total internal reflection fluorescence (TIRF) module. To extend the imaging depth, the system was slightly

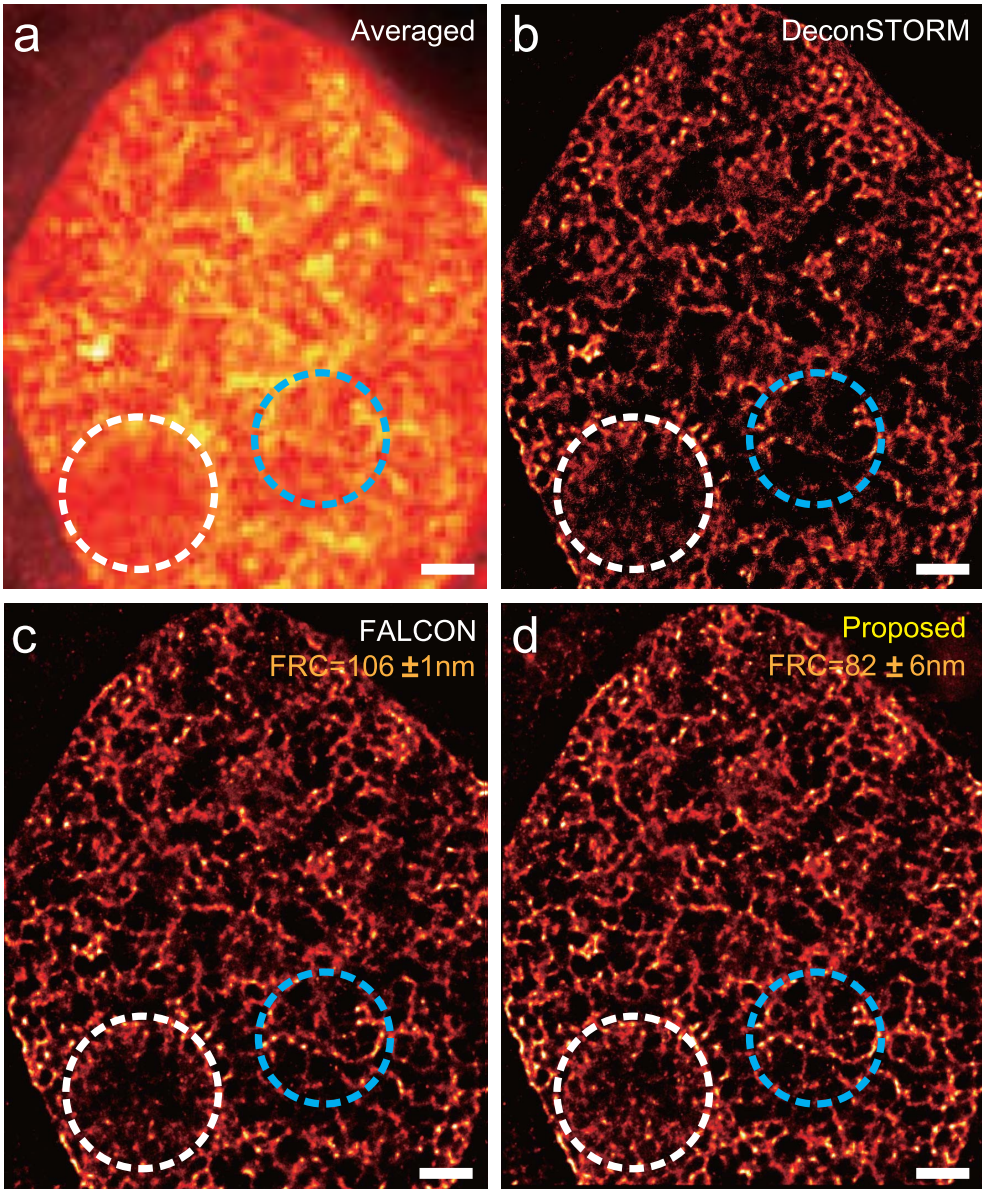

Fig. 6. Experimental results of live-cell imaging data. U2OS cells was prepared, and the nuclei of the cells were labeled with Picogreen. (a) A conventional diffraction-limited wide-field microscopy image constructed by accumulating 2000 raw frames. (b) A DeconSTORM image. (c-d) SR images reconstructed by FALCON and the proposed method, respectively. Scale bars are 2 μm in (a-d).

modified using the HILO illumination [13], [48]. This results in PSF variations within the depth of focus that needed to be corrected, and the validity of correcting PSF variation using the Gaussian PSF model is discussed in Appendix. A 488 nm laser (Sapphire 488 50, Coherent, Santa Clara, CA) used to excite the Picogreen was focused on the back focal plane of the oil-immersion objective (alpha Plan-Apochromat, 100x, NA = 1.46; Zeiss). The fluorescent light collected by this objective then was projected onto an EMCCD camera (iXon+; Andor, Belfast, UK). Additional lenses resulted in a final image pixel size of 100 nm. In this setup, 2000 raw images were acquired at a camera acquisition of 33.3 Hz rate with a laser excitation intensity of 15 kW cm^{-2}, resulting in high molecular activation.

The live-cell data was processed by the proposed algorithm for comparison with the other two HD localization algorithms. For the proposed method, locally estimated PSFs were used, and every two consecutive frames were processed together in the deconvolution step. Because the other two methods used the fixed PSF model, the average FWHM of the PSFs was applied to these methods. Moreover, we ran DeconSTORM while also assuming that the average activation length of the molecules is two frames.

The reconstructed SR images are shown in Fig. 6. We found that the proposed method detected 30% more probes than FALCON and also provided better SR imaging than the other methods. Particularly, it retained the connected structure, as highlighted by the blue and white dotted circles in Fig. 6 (a-d), while other methods missed this part. Moreover, the proposed method and FALCON were quantitatively compared by using a method based on Fourier ring correlation (FRC) [46], which was developed specifically for resolution assessment in localization microscopy. Because the image-based DeconSTORM approach is not

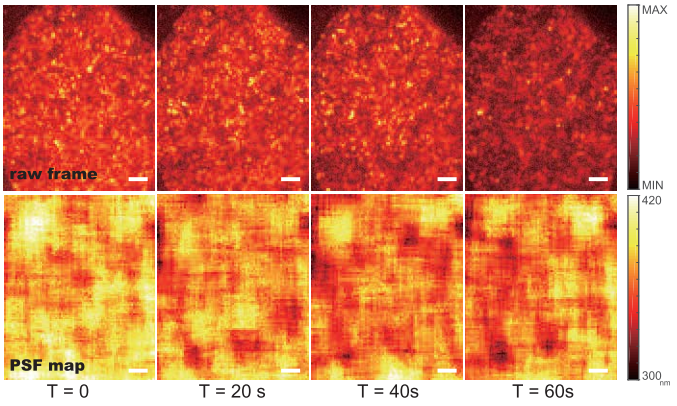

Fig. 7. Results of adaptive PSF estimation with live-cell imaging data. (top) High-density raw camera images acquired during 60 seconds, and (bottom) the widths of locally estimated PSFs in terms of FWHM. PSFs were estimated at each local patch. Scale bars are 2 μm in (a-d).

compatible with this evaluation method given the requirement of localized positions, it was excluded. In the FRC analysis, it was shown that the proposed method leads to improved spatial resolutions by 20% compared to those by FALCON.

In order to demonstrate space-time varying PSFs in live-cell image data, our adaptive PSF estimation was applied. Specifically, the width of PSF was locally estimated from each local patch of 45 $\times$ 45 pixels. In Fig. 7, the estimated widths of the PSFs were visualized in terms of the FWHM. The results showed slight spatio-temporal variation of the PSFs. Considering the prolonged acquisition time approximately 60 seconds, the relatively large nuclei stained by PicoGreen and the longer depth of field of our modified TIRF setup, it was deemed reasonable to expect z-directional fluctuations of the fluorophore locations around the nuclei area due to the cell mobility. We also observed that the widths of the PSFs decreased after 60 sec. This may have originated either from algorithmic bias due to the lower data SNR from photobleaching or changes in the imaging environments from the movement of the cell nuclei or from a stage drift. However, considering the resolution improvement in Fig. 6 by the proposed method, we conjecture that the PSF estimation was useful in this experiment.

To evaluate grid-free localization specifically, the proposed method was compared with another grid-free method FALCON using Taylor approximation of the PSF. For this analysis, every localization location was converted into the relative displacement toward the center of the nearest pixel, which is displayed as a histogram, as shown in Fig. 8. This shows that the histograms of the proposed method have more uniform distributions than those of FALCON. In particular, the non-uniformity observed in the FALCON reconstruction is distinct at every one third of the pixel position, which is the size of sub-pixel grid of FALCON. This occurs because Taylor approximation errors in FALCON induce local bias, resulting in the non-uniformity of the histograms. In addition, the Taylor approximation errors increase when an inaccurate PSF model is used. Finally, the counts in the histogram of Fig. 8 clearly show that more probes are detected by the proposed method compared to FALCON.

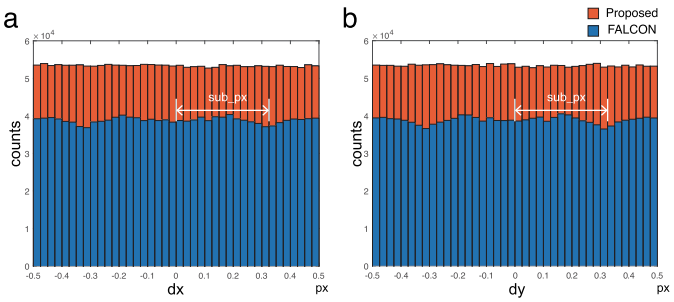

Fig. 8. Histograms of relative localization offsets. Each localization location was converted relative to the center of nearest pixel in (a) x-direction, and (b) y-direction, respectively.

VI. Discussion

Note that there are several hyper-parameters in the proposed algorithm, which includes λ, α, μ as well as a re-initialization parameter. However, in our experiments, we found that the algorithm was not overly sensitive to α, μ or a re-initialization. Specifically, we found that the proposed method works properly in our experiments for $\alpha \in [10^{-3}, 10^{-1}]$ and $\mu \in [10^{-5}, 10^{-4}]$. Thus, we choose the default values of α and μ (10^{-2} and 10^{-4}, respectively). However, we found that the regularization parameter λ was important. Because the regularization parameter λ in the deconvolution step determines the sparsity level, the sensitivity of this parameter was analyzed in various imaging conditions by varying the brightness of the photons and the fluorophore density. Specifically, with the simulated data sets in Fig. 3, we measured localization accuracy with several values of λ in terms of the recall rates, localization accuracy, and false-positive ratio, as shown in Fig. 9. The results showed that $\lambda = 20$ was a good choice to balance the detection ability and localization accuracy of the data set. Moreover, it was relatively insensitive to the SNR of the data because it showed the similar trends in both low- and high- SNR conditions. Moreover, it can be adjusted according to user preference between recall and precision.

Poisson modeling should be used with special attention paid to preprocessing and converting the analog-digital units (ADUs) into physical photon units. While this can often be omitted in routine experiments, without careful scale calibration the data may not follow the Poisson-like noise statistics, resulting in poor reconstruction. Therefore, in this paper, the gain of the camera was carefully calibrated to reconstruct and analyze HD data. Note that this gain calibration is also important for other HD algorithms using Gaussian noise model.

Because the proposed method has been specifically developed for the 2D imaging problem, it is basically limited to shallow imaging whose PSF can be still modeled by Gaussian. Accordingly, it is recommended to work with modified TIRF-based systems [13], [48]. However, our method can be extended to 3D SR imaging techniques such as the astigmatic [49], biplane imaging [50] or hybrid [10] type. In such case, the deconvolution should be performed in the 3D Fourier space and more realistic PSF model, and 3D harmonic retrieval [51], [52] should be considered.

In terms of computational complexity, our grid-free localization algorithm is formulated in a smaller dimension compared

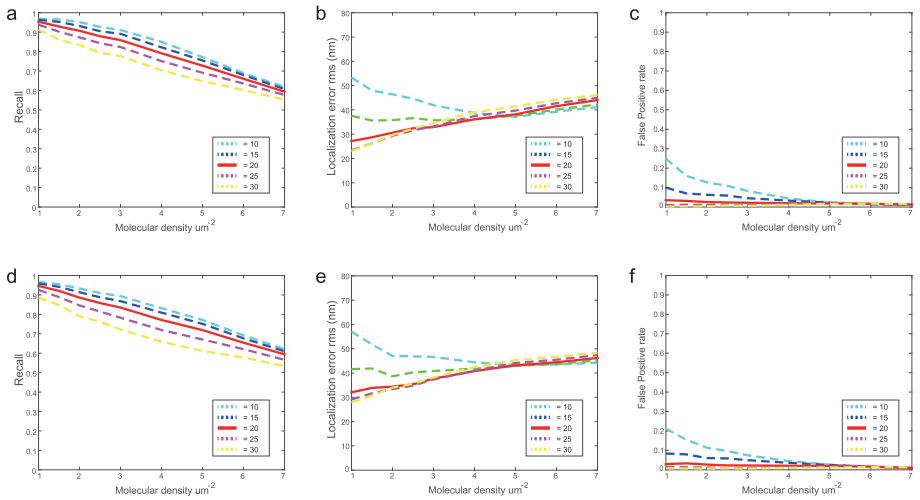

Fig. 9. Parameter (λ) sensitivity analysis on high and low SNR simulated data. (a) Molecular recall rates, (b) localization accuracy, and (c) false positive localization ratio with λ of 10, 15, 20, 25, 30 for the high SNR simulated data. (d) Recall rates, (e) localization accuracy, and (f) false positive localization ratio with respect to λ of 10, 15, 20, 25, 30 for the low SNR simulated data.

to existing HD localization methods using a fine sub-pixel grid with a downsampling factor of 3x or 5x. Specifically, the proposed method uses the same grid of raw camera data such that the dimension of the problem can be reduced down to the square of the down-sampling factor. Unfortunately, we do not claim that the current implementation is computationally advantageous compared to some existing softwares. For example, our algorithm has a processing time similar to that of DeconSTORM, but it is not as fast as FALCON. Specifically, our independent Matlab implementations of three methods on a graphic processing unit (GPU) (Nvidia GTX Titan, Maxwell architecture), the proposed method, DeconSTORM and FALCON took 45 msec, 48 msec and 4 msec, respectively, to reconstruct a μm^2 area. The processing times of all three methods are mostly determined by the sizes of processed regions, not the density level of the activated molecules. Two-frame processing of the proposed method has a slightly longer run time of $52 msec/\mu m^2$. Although there is also room for improvement by optimizing the implementation, the main computational bottleneck of the proposed algorithm is the rank minimization step for relatively large-scale Hankel matrices. However, we expect that this problem will be mitigated by integration with the latest development in rank minimization from the optimization community. For example, we can directly use an annihilating filter [53] rather than using the high-dimensional Hankel matrix.

VII. Conclusion

In the present work, we proposed a new grid-free super-resolution microscopy algorithm using annihilating filter-based low-rank Hankel structure matrix approach. The algorithm was developed based on the observation that sparsity in the image space is directly linked to a low-rank property in the Fourier domain. Accordingly, we converted our multiple source localization problem into a harmonic retrieval problem by initially undertaking the deconvolution in the Fourier domain and then extracting the frequency harmonics, from which the spatial locations are directly calculated.

Moreover, we proposed a parametric PSF estimation method for 2D deconvolution using the low-rank property of the weighted Hankel matrix, with the method validated by numerical studies. Furthermore, our deconvolution algorithm not only utilizes a realistic Poisson noise model but also the temporal redundancy of the signal by imposing a low-rank on the concatenated Hankel matrices of several frames. In addition, the matrix pencil-based harmonic retrieval algorithm allows for truly continuous localization. The entire process was done in a patch-by-patch manner, resulting in spatially adaptive localizations.

The proposed method was validated using simulated and experimental high-density dSTORM data for live-cell imaging. Specifically, the ability to detect molecules in a low-SNR environment was significantly enhanced compared to previous HD algorithms. In addition, the localization accuracy was significantly improved quantitatively in both numerical and experimental studies by applying our true grid-free localization, data-adaptive PSF estimation and multi-frame deconvolution. Therefore, we believe that the proposed method will be a very powerful tool for those conducting quantitative biological research in the area of live-cell imaging.

Appendix

Generally, PSFs in biological samples vary spatially [54]–[56] and temporally [57], [58] due to induced aberrations and light scattering within the samples. The aberrations are induced not only by the refractive index mismatch between a sample and the imaging medium, but also by intrinsic variations of the sample. Accordingly, PSF model such as Gibson and Lanni (GL) model [59] has been often used, since it considers the aberrations. Specifically, GL PSF model takes into account refractive index mismatches between the immersion, cover-slip and sample layers, so we believe it is a realistic model. Thus, we validated the effectiveness of our Gaussian PSF model compared to GL model PSF (GL PSF). Specifically, we have generated GL PSFs over a large axial range from $-1\mu m$ to

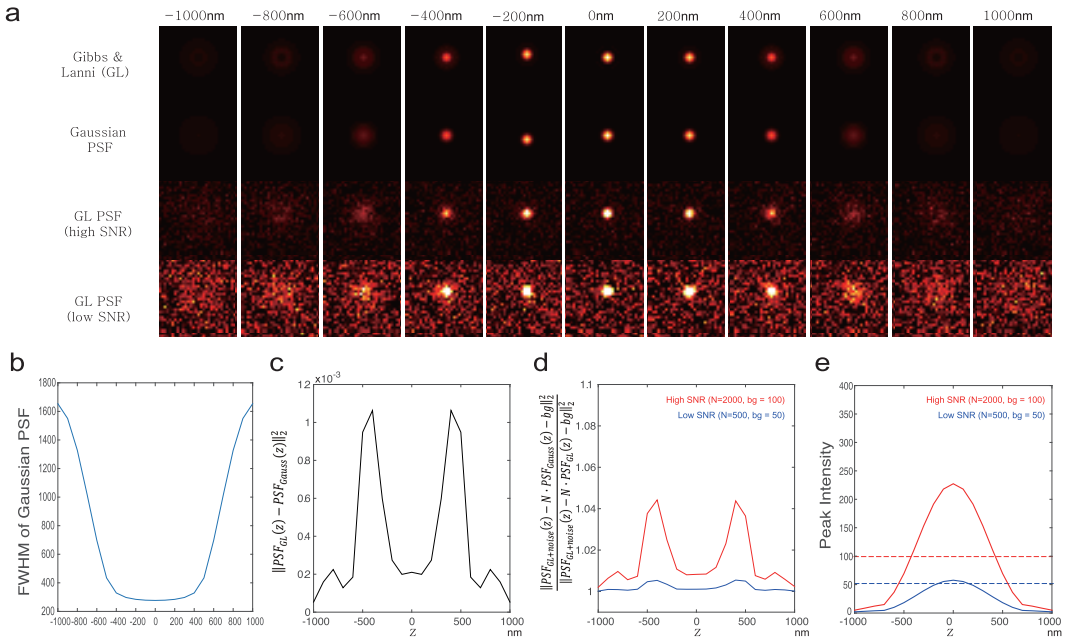

Fig. 10. Gaussian PSF error analysis: (a) visualization of Gibson & Lanni PSF (GL PSF), Gaussian PSF, and GL PSFs at two SNR levels. The Poisson noises are added by assuming that the intensity of a source and background signal (N, bg) are (2000,100) in the case of high SNR and (500,50) in the case of low SNR. (b) The FWHMs of the Gaussian PSFs that best fit the GL PSFs. (c) The least-square fit errors between Gaussian PSF and GL PSF. (d) Relative localization error of Gaussian PSF with respect to GL PSF at two SNR levels. (e) Peak intensities in noisy GL PSFs of (a).

$1\mu m$ using the ImageJ plugin [60]. In Fig. 10(a), GL PSFs and Gaussian PSFs are visualized with the width of each Gaussian PSF chosen to minimize the least squares error toward the corresponding GL PSF. With the camera noise, we could not find the difference between the two models in their forms. Moreover, Fig. 10(b) shows that the width of Gaussian PSF in the focus range $(-400nm \sim 400nm)$ varies slightly and increases rapidly in the out-of-the focus area. In Fig. 10(c), we also plot the fitting error between the normalized Gaussian PSF and the GL PSF, which has peaks around $\pm 500nm$. To analyze how much this model mismatch affects localization performance, we conducted simulation studies under shot noise and GL PSF model at two noise levels. Specifically, for a high SNR simulation we assume source intensity and background signal are (2000,100), while they are set to (500,20) in the case of a low SNR. Then, localization was performed using GL PSF and Gaussian PSF. In the relative error plot in Fig. 10(d), we can see that the fit error using Gaussian PSF was slightly larger than the fitting error by the true one (GL PSF). However, the relative error is only up to 5% in the case of high SNR, while it is less than 1% in the case of low SNR. This suggests that the effect of the model mismatch between Gaussian and GL PSFs has limited effects on localization accuracy. Considering other physical properties such as scattering, the mismatch can be negligible. Therefore, we believe that the Gaussian PSF model with varying width is sufficiently accurate for our purpose.

In our setup that uses HILO illumination, the illumination thickness is about $3\mu m$ [61], and the depth of focus of our objective lens is approximately 700 nm. In spite of this, we claim that our experimental setup is adequate for 2D single molecule imaging within the depth of focus. In order to prove that the tilted HILO illumination in our setup poses no problems, we performed an additional numerical study to examine the peak intensity value of PSFs located around the focal plane. To that end, we considered noiseless GL-PSFs weighted by the source intensity to which we added the background signal. Then, we plot the peak intensity value of the PSFs as solid lines with the corresponding background signal as dashed lines in the case of low and high SNR images. The results were recorded as red at high SNR case and blue at low SNR case. In Fig. 10(e), we can see that the peak intensity becomes quickly smaller than the background, especially at low SNR. This suggests that the signatures of PSFs from out of focus area are negligible and undistinguishable from the background signal. Therefore, we believe that despite the HILO illumination, our localization mechanism only picks up the point sources situated within the depth of focus: that is, those for which the Gaussian PSF model is adequate. Therefore, we believe that our Gaussian PSF model is good for 2D localization under HILO illumination.

ACKNOWLEDGMENT

The authors thank Alexander Benke, Lina Carlini and Prof. Suliana Manley in Laboratory of Experimental Biophysics (LEB) at EPFL to acquire the experimental data and to have productive discussions on this work. The authors also thank Prof. Jung-Hoon Park at the Ulsan National Inst. of Science and Technology (UNIST) for useful discussion and advices on adaptive optics.

REFERENCES

[1] M. J. Rust, M. Bates, and X. Zhuang, "Sub-diffraction-limit imaging by stochastic optical reconstruction microscopy (STORM)," *Nature Methods*, vol. 3, no. 10, pp. 793–796, 2006.

[2] S. T. Hess, T. P. K. Girirajan, and M. D. Mason, "Ultra-high resolution imaging by fluorescence photoactivation localization microscopy," *Biophys. J.*, vol. 91, no. 11, pp. 4258–4272, 2006.

[3] E. Betzig *et al.*, "Imaging intracellular fluorescent proteins at nanometer resolution," *Science*, vol. 313, no. 5793, pp. 1642–1645, 2006.

[4] S. J. Holden, S. Uphoff, and A. N. Kapanidis, "DAOSTORM: An algorithm for high-density super-resolution microscopy," *Nature Methods*, vol. 8, no. 4, pp. 279–280, 2011.

[5] F. Huang, S. L. Schwartz, J. M. Byars, and K. A. Lidke, "Simultaneous multiple-emitter fitting for single molecule super-resolution imaging," *Biomed. Opt. Express*, vol. 2, no. 5, pp. 1377–1393, 2011.

[6] L. Zhu, W. Zhang, D. Elnatan, and B. Huang, "Faster STORM using compressed sensing," *Nature Methods*, vol. 9, no. 7, pp. 721–723, Apr. 2012.

[7] E. A. Mukamel, H. Babcock, and X. Zhuang, "Statistical deconvolution for superresolution fluorescence microscopy," *Biophys. J.*, vol. 102, no. 10, pp. 2391–2400, May 2012.

[8] K. Kim *et al.*, "Fast maximum likelihood high-density low-snr super-resolution localization microscopy," in *Proc. 10th Int. Conf. Sampling Theory Appl. (SampTA)*. Bremen, Germany: Jacobs Univ., 2013, pp. 285–288.

[9] J. Min *et al.*, "FALCON: Fast and unbiased reconstruction of high-density super-resolution microscopy data," *Sci. Rep.*, vol. 4, Apr. 2014, Art. no. 4577.

[10] J. Min, S. J. Holden, L. Carlini, M. Unser, S. Manley, and J. C. Ye, "3D high-density localization microscopy using hybrid astigmatic/biplane imaging and sparse image reconstruction," *Biomed. Opt. Express*, vol. 5, no. 11, pp. 3935–3948, 2014.

[11] J. Huang, K. Gumpper, Y. Chi, M. Sun, and J. Ma, "Fast two-dimensional super-resolution image reconstruction algorithm for ultra-high emitter density," *Opt. Lett.*, vol. 40, no. 13, pp. 2989–2992, 2015.

[12] J. Huang, M. Sun, J. Ma, and Y. Chi, "Super-resolution image reconstruction for high-density 3D single-molecule microscopy," in *Proc. IEEE 13th Int. Symp. Biomed. Imag. (ISBI)*, Apr. 2016, pp. 241–244.

[13] M. Tokunaga, N. Imamoto, and K. Sakata-Sogawa, "Highly inclined thin illumination enables clear single-molecule imaging in cells," *Nature Methods*, vol. 5, no. 2, pp. 159–161, 2008.

[14] J. C. Ye, J. M. Kim, K. H. Jin, and K. Lee, "Compressive sampling using annihilating filter-based low-rank interpolation," *IEEE Trans. Inf. Theory*, vol. 63, no. 2, pp. 777–801, Feb. 2017.

[15] K. H. Jin, D. Lee, and J. C. Ye, "A general framework for compressed sensing and parallel MRI using annihilating filter based low-rank Hankel matrix," *IEEE Trans. Comput. Imag.*, vol. 2, no. 4, pp. 480–495, Dec. 2016.

[16] Y. Chen and Y. Chi, "Robust spectral compressed sensing via structured matrix completion," *IEEE Trans. Inf. Theory*, vol. 60, no. 10, pp. 6576–6601, Oct. 2014.

[17] J. Lee, K. H. Jin, and J. C. Ye, "Reference-free single-pass EPI Nyquist ghost correction using annihilating filter-based low rank Hankel matrix (ALOHA)," *Magn. Reson. Med.*, vol. 76, no. 6, pp. 1775–1789, Dec. 2016, doi: 10.1002/mrm.26077.

[18] D. Lee, K. H. Jin, E. Y. Kim, S.-H. Park, and J. C. Ye, "Acceleration of MR parameter mapping using annihilating filter-based low rank Hankel matrix (ALOHA)," *Magn. Reson. Med.*, vol. 76, no. 6, pp. 1848–1864, Dec. 2016, doi: 10.1002/mrm.26081.

[19] K. H. Jin, J.-Y. Um, D. Lee, J. Lee, S.-H. Park, and J. C. Ye, "MRI artifact correction using sparse + low-rank decomposition of annihilating filter-based Hankel matrix," *Magn. Reson. Med.*, vol. 78, no. 1, pp. 327–340, 2017.

[20] G. Ongie and M. Jacob, "Off-the-grid recovery of piecewise constant images from few Fourier samples," *SIAM J. Imag. Sci.*, vol. 9, no. 3, pp. 1004–1041, 2015.

[21] M. Mani, M. Jacob, D. Kelley, and V. Magnotta, "Multi-shot sensitivity-encoded diffusion data recovery using structured low-rank matrix completion (MUSSELS)," *Magn. Reson. Med.*, vol. 78, no. 2, pp. 494–507, Aug. 2017.

[22] K. H. Jin and J. C. Ye, "Annihilating filter-based low-rank Hankel matrix approach for image inpainting," *IEEE Trans. Image Process.*, vol. 24, no. 11, pp. 3498–3511, Nov. 2015.

[23] K. H. Jin and J. C. Ye, "Sparse and low-rank decomposition of a Hankel structured matrix for impulse noise removal," *IEEE Trans. Image Process.*, vol. 27, no. 3, pp. 1448–1461, 2018.

[24] X. Qu, M. Mayzel, J.-F. Cai, Z. Chen, and V. Orekhov, "Accelerated NMR spectroscopy with low-rank reconstruction," *Angew. Chem. Int. Ed.*, vol. 54, no. 3, pp. 852–854, Jan. 2015.

[25] K. H. Jin, J. Min, and J. C. Ye, "Patch based low rank structured matrix completion for accelerated scanning microscopy," in *Proc. IEEE 12th Int. Symp. Biomed. Imag. (ISBI)*, Apr. 2015, pp. 1236–1239.

[26] K. H. Jin, Y. S. Han, and J. C. Ye, "Compressive dynamic aperture B-mode ultrasound imaging using annihilating filter-based low-rank interpolation," in *Proc. IEEE 13th Int. Symp. Biomed. Imag. (ISBI)*, Apr. 2016, pp. 1009–1012.

[27] M. Vetterli, P. Marziliano, and T. Blu, "Sampling signals with finite rate of innovation," *IEEE Trans. Signal Process.*, vol. 50, no. 6, pp. 1417–1428, Jun. 2002.

[28] I. Maravić and M. Vetterli, "Exact sampling results for some classes of parametric nonbandlimited 2-D signals," *IEEE Trans. Signal Process.*, vol. 52, no. 1, pp. 175–189, Jan. 2004.

[29] I. Markovsky and K. Usevich, "Structured low-rank approximation with missing data," *SIAM J. Matrix Anal. Appl.*, vol. 34, no. 2, pp. 814–830, 2013.

[30] M. Fazel, T. Pong, D. Sun, and P. Tseng, "Hankel matrix rank minimization with applications to system identification and realization," *SIAM J. Matrix Anal. Appl.*, vol. 34, no. 3, pp. 946–977, 2013.

[31] Y. Chen and Y. Chi, "Spectral compressed sensing via structured matrix completion," in *Proc. ICML*, 2013, pp. 414–422.

[32] P. J. Shin *et al.*, "Calibrationless parallel imaging reconstruction based on structured low-rank matrix completion," *Magn. Reson. Med.*, vol. 72, no. 4, pp. 959–970, 2014.

[33] F. Vanpoucke, M. Moonen, and Y. Berthoumieu, "An efficient subspace algorithm for 2-D harmonic retrieval," in *Proc. IEEE Int. Conf. Acoust., Speech, Signal Process. (ICASSP)*, vol. 4, Apr. 1994, pp. IV/461–IV/464.

[34] Y. Hua, "Estimating two-dimensional frequencies by matrix enhancement and matrix pencil," *IEEE Trans. Signal Process.*, vol. 40, no. 9, pp. 2267–2280, Sep. 1992.

[35] M. A. T. Figueiredo and J. M. Bioucas-Dias, "Restoration of Poissonian images using alternating direction optimization," *IEEE Trans. Image Process.*, vol. 19, no. 12, pp. 3133–3145, Dec. 2010.

[36] M. Signoretto, V. Cevher, and J. A. Suykens, "An SVD-free approach to a class of structured low rank matrix optimization problems with application to system identification," in *Proc. IEEE Conf. Decis. Control*, 2013, paper EPFL-CONF-184990.

[37] N. Srebro, "Learning with matrix factorizations," Ph.D. dissertation, Dept. Elect. Eng. Comput. Sci., Massachusetts Inst. Technol., Cambridge, MA, USA, 2004.

[38] S. Boyd, N. Parikh, E. Chu, B. Peleato, and J. Eckstein, "Distributed optimization and statistical learning via the alternating direction method of multipliers," *Found. Trends Mach. Learn.*, vol. 3, no. 1, pp. 1–122, Jan. 2011.

[39] M. Hong and Z.-Q. Luo. (2012). "On the linear convergence of the alternating direction method of multipliers." [Online]. Available: https://arxiv.org/abs/1208.3922

[40] M. Hong, Z.-Q. Luo, and M. Razaviyayn, "Convergence analysis of alternating direction method of multipliers for a family of nonconvex problems," *SIAM J. Optim.*, vol. 26, no. 1, pp. 337–364, 2016.

[41] G. Li and T. K. Pong, "Global convergence of splitting methods for nonconvex composite optimization," *SIAM J. Optim.*, vol. 25, no. 4, pp. 2434–2460, 2015.

[42] R. Roy and T. Kailath, "Esprit-estimation of signal parameters via rotational invariance techniques," *IEEE Trans. Acoust., Speech, Signal Process.*, vol. 37, no. 7, pp. 984–995, Jul. 1989.

[43] J. M. Kim, O. K. Lee, and J. C. Ye, "Compressive MUSIC: Revisiting the link between compressive sensing and array signal processing," *IEEE Trans. Inf. Theory*, vol. 58, no. 1, pp. 278–301, Jan. 2012.

[44] J. Min *et al.*, "Fluorescent microscopy beyond diffraction limits using speckle illumination and joint support recovery," *Sci. Rep.*, vol. 3, Jun. 2013, Art. no. 2075.

[45] D. Sage *et al.*, "Quantitative evaluation of software packages for single-molecule localization microscopy," *Nature Methods*, vol. 12, no. 8, pp. 717–724, 2015.

[46] R. P. J. Nieuwenhuizen *et al.*, "Measuring image resolution in optical nanoscopy," *Nature Methods*, vol. 10, no. 6, pp. 557–562, 2013.

[47] S. van de Linde, "Direct stochastic optical reconstruction microscopy with standard fluorescent probes," *Nature Protocols*, vol. 6, no. 7, pp. 991–1009, 2011.

[48] S. J. Holden, T. Pengo, K. L. Meibom, C. F. Fernandez, J. Collier, and S. Manley, "High throughput 3D super-resolution microscopy reveals *Caulobacter crescentus in vivo* Z-ring organization," *Proc. Nat. Acad. Sci. USA*, vol. 111, no. 12, pp. 4566–4571, 2014.
[49] B. Huang, W. Wang, M. Bates, and X. Zhuang, "Three-dimensional super-resolution imaging by stochastic optical reconstruction microscopy," *Zhuang*, vol. 319, no. 5864, pp. 810–813, 2008.
[50] M. F. Juette *et al.*, "Three-dimensional sub–100 nm resolution fluorescence microscopy of thick samples," *Nature Methods*, vol. 5, no. 6, pp. 527–529, 2008.
[51] B. Aksasse, M. El Ansari, Y. Berthoumieu, and M. Najim, "High resolution 3D spectral method estimation," in *Proc. 11th Eur. Signal Process. Conf.*, Sep. 2002, pp. 1–4.
[52] M. Haardt, F. Roemer, and G. D. Galdo, "Higher-order SVD-based subspace estimation to improve the parameter estimation accuracy in multidimensional harmonic retrieval problems," *IEEE Trans. Signal Process.*, vol. 56, no. 7, pp. 3198–3213, Jul. 2008.
[53] G. Ongie and M. Jacob, "A fast algorithm for structured low-rank matrix recovery with applications to undersampled MRI reconstruction," in *Proc. IEEE 13th Int. Symp. Biomed. Imag. (ISBI)*, Apr. 2016, pp. 522–525.
[54] M. Schwertner, M. J. Booth, M. A. A. Neil, and T. Wilson, "Measurement of specimen-induced aberrations of biological samples using phase stepping interferometry," *J. Microsc.*, vol. 213, no. 1, pp. 11–19, 2004.
[55] M. Schwertner, M. J. Booth, and T. Wilson, "Characterizing specimen induced aberrations for high na adaptive optical microscopy," *Opt. Express*, vol. 12, no. 26, pp. 6540–6552, 2004.
[56] J. Zeng, P. Mahou, M.-C. Schanne-Klein, E. Beaurepaire, and D. Débarre, "3D resolved mapping of optical aberrations in thick tissues," *Biomed. Opt. Express*, vol. 3, no. 8, pp. 1898–1913, 2012.
[57] N. Olivier, D. Débarre, and E. Beaurepaire, "Dynamic aberration correction for multiharmonic microscopy," *Opt. Lett.*, vol. 34, no. 20, pp. 3145–3147, 2009.
[58] K. Kim, S. Lee, J. Yoon, J. Heo, C. Choi, and Y. Park, "Three-dimensional label-free imaging and quantification of lipid droplets in live hepatocytes," *Sci. Rep.*, vol. 6, Nov. 2016, Art. no. 36815.
[59] S. F. Gibson and F. Lanni, "Diffraction by a circular aperture as a model for three-dimensional optical microscopy," *J. Opt. Soc. Amer. A, Opt. Image Sci.*, vol. 6, no. 9, pp. 1357–1367, 1989.
[60] H. Kirshner, D. Sage, and M. Unser, "3D PSF models for fluorescence microscopy in ImageJ," in *Proc. 12th Int. Conf. Methods Appl. Fluorescence Spectrosc., Imag. Probes (MAF)*, 2011, p. 154.
[61] Z. Liu, L. D. Lavis, and E. Betzig, "Imaging live-cell dynamics and structure at the single-molecule level," *Mol. Cell*, vol. 58, no. 4, pp. 644–659, 2015.

Junhong Min received the B.S. degree from the School of Information and Communication, Hanyang University, Seoul, South Korea, in 2010, and the M.S. and Ph.D. degrees from the Department of Bio and Brain Engineering, Korea Advanced Institute of Science and Technology, Daejeon, South Korea, in 2012 and 2016, respectively. In 2012, he joined the Biomedical Imaging Group, École polytechnique fédérale de Lausanne, Switzerland, as a Visiting Research Student. He is currently a Senior Researcher with the Global Technology Center, Samsung Electronics Co. Ltd. His current research interests include big data analysis, machine learning, computer vision, and signal processing for industrial robot and manufacturing systems. He received the student's best paper awards at the 2013 IEEE Symposium on Biomedical Imaging. He was the Second Winner at the 2016 Low Dose CT Grand Challenge organized by the American Association of Physicists in Medicine with the world's first deep learning algorithm for low-dose CT.

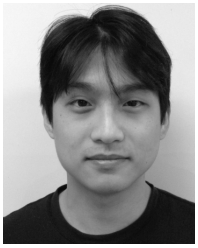

Kyong Hwan Jin received the B.S. degree and the integrated M.S. and Ph.D. degrees from the Department of Bio and Brain Engineering, Korea Advanced Institute of Science and Technology (KAIST), Daejeon, South Korea, in 2008 and 2015, respectively. He was a Post-Doctoral Scholar with KAIST from 2015 to 2016.

He is currently a Post-Doctoral Scholar with the Biomedical Imaging Group, École polytechnique fédérale de Lausanne, Switzerland. His research interests include low rank matrix completion, sparsity promoted signal recovery, sampling theory, biomedical imaging, and image processing in various applications.

Michael Unser (M'89–SM'94–F'99) is currently a Professor and the Director of the Biomedical Imaging Group, École polytechnique fédérale de Lausanne, Lausanne, Switzerland. He has authored the book with P. Tafti: *An Introduction to Sparse Stochastic Processes*," (Cambridge University Press, 2014). His primary area of investigation is biomedical image processing. He is internationally recognized for his research contributions to sampling theory, wavelets, the use of splines for image processing, stochastic processes, and computational bioimaging. He has authored over 300 journal papers on those topics. He is currently a member of the editorial boards of the *SIAM Journal on Imaging Sciences*, the IEEE JOURNAL SELECTED TOPICS IN SIGNAL PROCESSING, and the *Foundations and Trends in Signal Processing*. He is a member of the Swiss Academy of Engineering Sciences. He received several international prizes including four IEEE-SPS best paper awards and two technical achievement awards from the 2008 IEEE SPS and the 2010 IEEE EMBS. From 1985 to 1997, he was with the Biomedical Engineering and Instrumentation Program, National Institutes of Health, Bethesda, MD, USA, conducting research on bioimaging. He was an Associate Editor-in-Chief of the IEEE TRANSACTIONS ON MEDICAL IMAGING from 2003 to 2005. He is the Founding Chair of the Technical Committee on Bio Imaging and Signal Processing of the IEEE Signal Processing Society. He became a EURASIP Fellow in 2009.

Jong Chul Ye (M'99–SM'13) received the B.Sc. and M.Sc. degrees from Seoul National University, South Korea, and the Ph.D. from Purdue University, West Lafayette. He was with Philips Research, NY, USA, and GE Global Research, NY, USA. He is currently an Endowed Chair Professor and a Professor with the Department of Bio/Brain Engineering and an Adjunct Professor with the Department of Mathematical Sciences, Korea Advanced Institute of Science and Technology, South Korea. He is an Elected Member of the IEEE SPS Technical Committee on Bio-Imaging and Signal Processing, IEEE EMBS Technical Committee on Biomedical Imaging and Image Processing, and IEEE SPS Special Interest Group on Computational Imaging. He served as an Editorial Board Member for the *Magnetic Resonance in Medicine*. He is currently an International Advisory Board Member of the *Physics in Medicine and Biology*. He served as an Associate Editor for the IEEE TRANSACTIONS ON IMAGE PROCESSING. He is an Associate Editor of the IEEE TRANSACTIONS ON COMPUTATIONAL IMAGING, the IEEE TRANSACTIONS ON MEDICAL IMAGING, and the *Journal of Electronic Imaging* and a Senior Editor of the *IEEE Signal Processing Magazine*.

His current research interests include machine learning, compressed sensing and statistical signal processing for various image reconstruction problems in various medical and bioimaging modalities such as MRI, CT, optics, ultrasound imaging, PET, and fNIRS. His group received the First Place at the 2009 Recon Challenge at the ISMRM Workshop, the Second Place at the 2016 Low Dose CT Grand Challenge organized by the American Association of Physicists in Medicine, and the Third Place at the 2017 CVPR NTIRE Challenge on example-based single image super-resolution. He was an Advisor of best student paper awards (first and runner-up) at the 2013 and 2016 IEEE Symposium on Biomedical Imaging.